

RESEARCH ARTICLE

EVAnalyzer: High content imaging for rigorous characterisation of single extracellular vesicles using standard laboratory equipment and a new open-source ImageJ/Fiji plugin

Melanie Schürz¹  | Joachim Danmayr² | Maria Jaritsch¹ | Eva Klinglmayr¹ |
 Heloisa Melo Benirschke¹ | Cristian-Tudor Matea¹ | Patrick Zimmerebner¹ |
 Jakob Rauter¹ | Martin Wolf³  | Fausto Gueths Gomes³ | Zdenek Kratochvil⁴ |
 Zbynek Heger⁴ | Andrew Miller^{4,5,6} | Thomas Heuser⁷ | Vesna Stanojlovic¹ |
 Jana Kiefer¹ | Tanja Plank¹ | Litty Johnson¹ | Martin Himly¹ | Constantin Blöchl¹ |
 Christian G. Huber¹ | Martin Hintersteiner⁸ | Nicole Meisner-Kober¹

¹Department of Biosciences and Medical Biology, Paris Lodron University Salzburg, Salzburg, Austria

²Department of Informatics and Mathematics, Fernuniversität Hagen, Hagen, Germany

³Cell Therapy Institute, Spinal Cord Injury and Tissue Regeneration Centre Salzburg (SCI-TReCS), Paracelsus Medical University (PMU), Salzburg, Austria

⁴Department of Chemistry and Biochemistry, Mendel University in Brno, Brno, Czech Republic

⁵Veterinary Research Institute, Brno, Czech Republic

⁶KP Therapeutics (Europe) sro., Brno, Czech Republic

⁷Vienna Biocentre Core Facilities, Vienna, Austria

⁸EvoBiotiX SA, Lugano, Switzerland

Correspondence

Nicole Meisner-Kober, Department of Biosciences and Medical Biology, Paris Lodron University Salzburg, Salzburg, Austria.
 Email: nicole.meisner-kober@plus.ac.at

Abstract

Extracellular vesicle (EV) research increasingly demands for quantitative characterisation at the single vesicle level to address heterogeneity and complexity of EV subpopulations. Emerging, commercialised technologies for single EV analysis based

Abbreviations: BCA, Bicinchnic acid; BSA, Bovine serum albumin; CM, Conditioned Medium; CPA, cholesteryl-PEG₃₅₀-aminoxy; CRISPR, Clustered Regularly Interspaced Short Palindromic Repeats; CTAB, Cetyltrimethylammonium bromide; DLS, Dynamic Light Scattering; DMEM, Dulbecco's Modified Eagles Medium; DODAG, *N,N'*-dioctadecyl-*N*-4,8-diaza-10-aminodecanoylglycine amide; DOPE, 1,2-dioleoyl-sn-glycero-3-phosphoethanolamine; dSTORM, Direct stochastic optical reconstruction microscopy; dUC, Differential ultracentrifugation; EGFP, Enhanced green fluorescent protein; emGFP, Emerald GFP; EV, Extracellular vesicle; FBS, Foetal bovine serum; FCS, Fluorescence Correlation Spectroscopy; Fiji, Fiji is Just ImageJ; FoV, Field of view; FP, Fluorescent protein; FPLC, Fast protein liquid chromatography; FRET, Fluorescence resonance energy transfer; GFP, Green fluorescent protein; GUI, Graphical user interface; HEK293T, Human Embryonic Kidney cells; IgG, Immune globulin G; IMFC, Imaging Flow Cytometry; LNP, Lipid-based nanoparticle; MEV, Milk EVs; MG, MemGlow; MIP, Maximum intensity projection; MS, Mass spectrometry; NGS, Normal goat serum; NHS, N-hydroxysuccinimide; NTA, Nanoparticle tracking analysis; ONI, Oxford Nanoimager; PAGE, Polyacrylamide gel electrophoresis; PBS, Phosphate buffered saline; PDA, Photodiodearray; Pdl, Polydispersity index; PEI, Polyethyleneimine; PFA, Paraformaldehyde; QG, Quartz glass; RAM, Random access memory; ROI, Region of interest; RP-HPLC, Reversed phase - High performance liquid chromatography; RT-qPCR, Reverse transcription - quantitative polymerase chain reaction; SD, Standard deviation; SDS, Sodium dodecyl sulfate; SEC, Size exclusion chromatography; SiO₂, NPSilica dioxide nanoparticle; siRNA, short interfering RNA; SOP, Standard operating procedure; STED, Stimulated emission depletion; TBS, Tris buffered saline; TEM, Transmission electron microscopy; TEOS, Tetraethyl-ortho-silicate; TFF, Tangential flow filtration; TH, Threshold; TIRF, Total Internal Reflection Microscopy; TMR, Tetramethylrhodamine; TMT, Tandem mass tag; TRPS, Tuneable resistive pulse sensing; TS, Tetraspek; UC, Ultracentrifugation; UF, Ultrafiltration; UV, Ultraviolet; WB, Western Blotting.

Melanie Schürz and Joachim Danmayr contributed equally.

This is an open access article under the terms of the [Creative Commons Attribution-NonCommercial-NoDerivs License](https://creativecommons.org/licenses/by-nc-nd/4.0/), which permits use and distribution in any medium, provided the original work is properly cited, the use is non-commercial and no modifications or adaptations are made.

© 2022 The Authors. *Journal of Extracellular Vesicles* published by Wiley Periodicals, LLC on behalf of the International Society for Extracellular Vesicles.

Funding information

H2020-EU.1.4. - EXCELLENT SCIENCE - Research Infrastructures, Grant/Award Number: 'NanoCommons'731032 and AF-IGA2021-IP057; European Regional Development Fund, Grant/Award Numbers: EVTT, EFRE/IWB 20102-F1900731-KZP; European Regional Development Fund, Grant/Award Numbers: OPVVV Project FIT, CZ.02.1.01/0.0/0.0/15_003/0000495; County of Salzburg, WISS2025, Grant/Award Number: 'EV-TTBPro', P1812596; County of Salzburg, WISS2025, Grant/Award Number: 'EVQuant'20102-F2100572-FPR; County of Salzburg, WISS2025, Grant/Award Number: 'STEB'S'F2000237-FIP; FWF, Grant/Award Number: W01213

on, for example, imaging flow cytometry or imaging after capture on chips generally require dedicated instrumentation and proprietary software not readily accessible to every lab. This limits their implementation for routine EV characterisation in the rapidly growing EV field. We and others have shown that single vesicles can be detected as light diffraction limited fluorescent spots using standard confocal and widefield fluorescence microscopes. Advancing this simple strategy into a process for routine EV quantitation, we developed 'EVAnalyzer', an ImageJ/Fiji (Fiji is just ImageJ) plugin for automated, quantitative single vesicle analysis from imaging data. Using EVAnalyzer, we established a robust protocol for capture, (immuno-)labelling and fluorescent imaging of EVs. To exemplify the application scope, the process was optimised and systematically tested for (i) quantification of EV subpopulations, (ii) validation of EV labelling reagents, (iii) *in situ* determination of antibody specificity, sensitivity and species cross-reactivity for EV markers and (iv) optimisation of genetic EV engineering. Additionally, we show that the process can be applied to synthetic nanoparticles, allowing to determine siRNA encapsulation efficiencies of lipid-based nanoparticles (LNPs) and protein loading of SiO₂ nanoparticles. EVAnalyzer further provides a pipeline for automated quantification of cell uptake at the single cell–single vesicle level, thereby enabling high content EV cell uptake assays and plate-based screens. Notably, the entire procedure from sample preparation to the final data output is entirely based on standard reagents, materials, laboratory equipment and open access software. In summary, we show that EVAnalyzer enables rigorous characterisation of EVs with generally accessible tools. Since we further provide the plugin as open-source code, we expect EVAnalyzer to not only be a resource of immediate impact, but an open innovation platform for the EV and nanoparticle research communities.

KEYWORDS

cell uptake, EV immunolabelling, exosomes, extracellular vesicles, lipid nanoparticles, liposomes, open innovation, silica nanoparticles, single particle imaging, single vesicle imaging

1 | INTRODUCTION

The biology of extracellular vesicles (EVs) is inherently linked to their complexity and heterogeneity at the single vesicle level (Mizenko et al., 2021; Willms et al., 2018). Current understanding suggests that cells not only secrete different classes of vesicles through distinct biogenesis pathways, but that even specific EV subtypes such as exosomes, derived from the same cell type through the same canonical biogenesis pathway, comprise a spectrum of individual vesicles when zooming in on the molecular level (Bordanaba-Florit et al., 2021). Protein machineries such as the ESCRT complexes (Colombo et al., 2013; Juan & Fürthauer, 2018) control the sorting of molecules into each individual vesicle. The repertoire of EV cargoes not only varies between cell types but dynamically changes with the state of the producing cell (Willms et al., 2018). This is exemplified in a recent study that made use of microfluidics to capture single cells, combined with Total Internal Reflection Microscopy (TIRF) for imaging of the vesicles after immunostaining (Nikoloff et al., 2021). This revealed that even an individual cell secretes a remarkably heterogeneous population of different vesicles under the same conditions and within a short time frame—illustrating the critical importance of quantitative information at the single vesicle level. The EV field is still young and resolving EV mechanisms to the molecular level will require a deepened understanding of single vesicle populations, beyond characterisation by classical ensemble averaging methods.

One possible solution for single vesicle visualisation and quantification is fluorescence microscopy. Tracking individual fluorescent vesicles by imaging was first reported by Tian et al. (2010) in a study which relied on lipophilic dyes to monitor EV ('exosome') uptake into live cells. We later used genetic reporters for unambiguous labelling of CD63-positive vesicles with fluorescent protein (FP) tags for resolving their cell uptake routes. This revealed that tetraspanin-FP labelling stoichiometries are sufficient for single vesicle detection on confocal microscopes, thereby enabling single vesicle quantification both *in vitro* as well as in live and fixed cells (Corso et al., 2019; Heusermann et al., 2016). Following this early work, fluorescence imaging of single vesicles, both by tetraspanin-reporters as well as immunolabelling, has been used increasingly in the field to track single EVs in cellular and *in vivo* models (e.g., Riazanski et al., 2022; Strohmeier et al., 2021; Sung et al., 2020; Verweij et al., 2021) as well as to quantify EV subpopulations. For example, Burbidge *et al.* reported on centrifugation mediated immobilisation of EVs

on microscope slides ('spinoculation') to characterise EV subpopulations after immunolabelling and high-resolution wide field deconvolution microscopy with image analysis by the Imaris software (Burbidge et al., 2020). Hartjes *et al.* described 3D confocal imaging of lipid-dye labelled EVs after embedding and immunostaining within a polyacrylamide gel. This assay potentially allows a quasi-solution measurement of EVs, however, a systematic validation as well as testing for more diverse samples is still required (Hartjes et al., 2020). Similar strategies have been reported elsewhere using more advanced technologies such as TIRF microscopy (Han et al., 2021; Martín-Cófreces et al., 2021) or single molecule localisation microscopy (Strohmeier et al., 2021) for in depth characterisation and tetraspanin profiling of single vesicles.

Specialist companies have also recognised the potential of single vesicle imaging for the EV community. Platforms for EV capture on chips and fluorescence-based detection using tetraspanin antibodies have recently been commercialised for example by NanoView or Oxford Nanoimaging. These platforms are increasingly used in EV studies (e.g., Melling et al., 2022; Tertel et al., 2020; Wolf et al., 2022) and are promising to make an impact for the field, although they generally require integrated instrumentation, software and consumables. Due to the significant initial investment, operation costs and required expert know-how, such technologies are primarily implemented in highly specialised EV labs but not readily accessible to all academic institutions, and also of limited access to community innovation.

Recently, we and others have demonstrated that single EVs can be visualised even with standard widefield microscopes and on regular quartz glass slides (Burbidge et al., 2020; Corso et al., 2019). This suggested that a straightforward, cheap and robust process could be devised for quantitative single vesicle analysis by standard fluorescence microscopy. It turned out that the bottleneck is not only in the sample preparation, but also in the automated quantification of multiple images with freely available software. Here we introduce 'EVAnalyzer', a Fiji (Fiji is just ImageJ) plugin for automated, quantitative single vesicle analysis from large sets of imaging data. Using this tool, we established a robust protocol for capture, (mmobi-)labelling and fluorescent imaging of EVs using exclusively standard reagents, materials and equipment. We provide EVAnalyzer as an open access / open-source code tool for the EV community after systematic validation with EVs from different sources, LNPs SiO₂ nanoparticles and using different labelling methods, and describe its use for key questions in EV research which require single vesicle quantification, ranging from EV sample characterisation to single cell / single vesicle uptake quantification.

2 | MATERIALS AND METHODS

2.1 | Plasmids

All expression constructs are described in Supplementary File 7. Fluorescent protein tagged human tetraspanins were cloned in pcDNA6.2 as described previously (Corso et al., 2019; Heusermann et al., 2016). Full length coding sequences of the bovine tetraspanins CD63 and CD81 (Genbank accession no NM_205803.1 and NM_001035099.1) fused to N-terminal mNeon were codon optimised for expression in human cells and purchased from GeneArt (Thermo Scientific, IL, USA) as insert in pcDNA 3.1. Restriction sites were introduced to flank the bovine CD63 sequence for subcloning. Human codon optimised bovine CD9 (Genbank accession no NM_173900.2) was purchased from GeneArt and subcloned into pcDNA3.1 by replacing the bovine CD63 mNeon insert using the introduced BamHI/ApaI restriction sites.

2.2 | Cell culture and preparation of conditioned medium

Human embryonic kidney cells (HEK293T) (ATCC) were cultured in Dulbecco's Modified Eagle's Medium High Glucose (DMEM, Gibco, MD, USA) supplemented with 10% foetal bovine serum (FBS, Gibco, MD, USA), 1% GlutaMAX Supplement 100x (Gibco, MD, USA) and 1% antibiotic/antimycotic (100x, Gibco, MD, USA) and incubated at 37°C, 5% CO₂ and 90% relative humidity. For cell transfection, 2×10^7 cells were seeded in T225 cell culture flasks (Falcon), left to attach overnight, washed with OptiMEM (Gibco, MD, USA) and then transfected with plasmids of interest complexed with branched polyethyleneimine (Sigma, MO, USA; 60 µg DNA: 90 µg PEI). 4 h after transfection, the medium was changed to OptiMEM supplemented with 1% Antibiotic/Antimycotic. Conditioned medium (CM) was harvested after 48 h of cultivation. For all transfection experiments performed throughout the manuscript, the ratio DNA: PEI is kept constant (1 µg DNA: 1.5 µg PEI).

Additionally, EVs were isolated from HEK293T cells stably expressing CD63-mNeon kindly provided by Dr. Samir El Andaloussi and Dr. Andre Görgens (Karolinska Institute, Stockholm, Sweden; (Corso et al., 2017; Dar et al., 2021), as well as from HEK293T cells with CRISPR-Cas9 mediated genomic integration of GFP into the CD63 locus ('CD63 CRISPR') or random genomic integration of CD63-GFP kindly provided by Dr. Mario Maierhofer (Fachhochschule Upper Austria, Linz, Austria; (Strohmeier et al., 2021)). Cells were cultured in DMEM supplemented with 10% FBS, 1% GlutaMAX and 1% Antibiotic/Antimycotic. For EV isolation, 2×10^7 cells were seeded in T225 flasks and, after cell attachment (overnight), medium was changed to OptiMEM supplemented with 1% Antibiotic/Antimycotic. CM was collected after 48 h of cultivation.

2.3 | Extracellular vesicle isolation from HEK293T cells

Conditioned Medium from transiently transfected or stable transgenic HEK293T cells was collected and centrifuged twice at 300xg for 5 min and once at 3000xg for 15 min. After filtration through a 0.22 μm filter, the filtrated CM was concentrated 50–100x via ultrafiltration (UF) using a 200 ml Amicon Stirred Cell over a 100 kDa MWCO filter. After a second 0.22 μm filtration step, 1 ml of the concentrate was loaded on a Superdex 20 Increase 10/30GL column (GE Healthcare, IL, USA) on a Shimadzu LC-20AI FPLC instrument equipped with a SPD-M20A Photodiode Array Detector (Shimadzu, Japan) and a RF-20A Fluorescence Detector (Shimadzu, Japan). The sample was eluted under isocratic conditions at 4°C and 0.8 ml/min using phosphate buffered saline (PBS: 8 g NaCl, 0.2 g KCl, 1.44 g Na_2HPO_4 , 0.24 g KH_2PO_4 per litre) adjusted to a pH of 7.4 and further filtered through a 0.22 μm filter. Fractions were pooled as indicated in Supplementary File 3 and concentrated 10–20x with a 10 kDa MWCO Amicon Ultra 4 ml centrifugal filter. The samples were stored at 4°C until further use.

2.4 | Isolation and labelling of extracellular vesicles from cow milk

Cow milk-derived extracellular vesicles (MEVs) were isolated as described elsewhere (De Groot et al., 2021). Briefly, after defatting, casein is removed by enzymatic coagulation and Evs are enriched by tangential flow filtration (TFF) in PBS with successively increasing molecular weight cut-offs. The EV isolation procedure was monitored by sampling at different intermediary steps and analysing the samples via size exclusion chromatography (SEC), nanoparticle tracking analysis (NTA) and total protein quantification using the bicinchoninic acid (BCA) Protein Assay Kit (Supplementary File 3). Next, the MEVs were fluorescently labelled at 1 nM in PBS for 1 h at 37°C simultaneously with 1000fold molar excess of each, Cy5 NHS ester (CAS No.: 1263093-76-0) and Cy7 NHS ester (CAS No.: 2408482-09-5) purchased from Lumiprobe GmbH (Hannover, Germany). The unbound excess fluorophores from the double labelled MEVs were removed via TFF (750 kDa cut-off), filtered through 0.22 μm modified polyethersulfone (mPES) membranes and stored at 4°C until further use.

2.5 | Protein concentration determination

Protein concentrations were either determined by BCA or Bradford measurements using commercial assays and following the manufacturer's instructions. For BCA measurements, the Pierce™ BCA Protein Assay Kit (Thermo Fisher Scientific, MA, USA) was used and the absorbance at $\lambda_{\text{max}} = 562$ nm was measured on a TECAN Spark multiplate reader. For protein quantification by Bradford, the Pierce Detergent Compatible Bradford Assay Kit (Thermo Fisher Scientific, MA, USA) was used and the absorbance at $\lambda_{\text{max}} = 595$ nm was measured on a NanoDrop 2000c Spectrophotometer (Thermo Scientific, MA, USA).

2.6 | Nanoparticle tracking analysis

Particle size distributions and concentrations were determined by nanoparticle tracking analysis (NTA) on a Nanosight LM14C equipped with a 488 nm laser (Malvern, UK) using the NTA analytical software version 3.1.54. Samples were diluted in their respective buffer and five videos (1 min each) were recorded with a camera level of 13–15 (12 for milk Evs), screen gain 1. Analysis software settings were kept constant for all measurements (detection threshold 5). For each sample, the mean of three individual measurements was calculated.

2.7 | Western blotting

Samples were mixed with SDS reducing buffer and separated on 4%–20% TGX Gels (BioRad, CA, USA) under reducing conditions in a SDS-containing electrode running buffer at pH 8.3. Proteins were transferred onto a 0.45 μm nitrocellulose membrane by semi dry blotting in a transfer buffer containing 10% methanol and blocked with TBS+ 0.2% Tween + 5% BSA (CD63, CD9, CD81) or TBS + 0.2% Tween + 2% non-fat dry milk (Tsg101) for 1 h at room temperature. The membranes were incubated with primary antibodies (CD63: abcam (UK) ab193349; TSG101: abcam (UK) ab83; CD9: Invitrogen (MA, USA) AHS0902; CD81: LA-B7247), diluted in the respective blocking buffer, overnight at 4°C on a rocker-shaker. Washing steps after primary and secondary antibody incubations were performed five times each with TBS + 0.2% Tween for 5 min. Secondary antibody (IRDye 680RD Goat anti-Mouse IgG), diluted in the respective blocking buffers, was incubated with the membranes for 1 h. The blots were imaged with the Licor system (Licor Odyssey FC Model 2800).

2.8 | Size exclusion chromatography (preparative and analytical)

Size exclusion chromatography (SEC) experiments were performed on a Shimadzu custom built system comprised of a mobile phase degassing unit (Shimadzu DGU-20A3R), three liquid chromatography pumps (Shimadzu Prominence LC-20Ai) a PDA detector (Shimadzu SPD-M20A) and a Fluorescence detector (Shimadzu RF-20A) with automated fraction collection (Shimadzu FRC-10A). The chromatographic system was mounted in a cold cabinet (Tritec, Hannover, DE) to ensure a constant temperature of 4°C during the runs. The Shimadzu LabSolutions software 5.97 was used for data acquisition, OriginPro 2020 9.70 was used for data analysis. All samples subjected to analytical (50 µl injection volume), or preparative (1 ml injection volume) SEC were fractionated on a dextran-agarose matrix column (Superdex® 200 Increase 10/300 GL, L × I.D. 30 cm × 10 mm, 8.6 µm) with isocratic elution at a flow of 0.8 ml/min. All samples were monitored by detection of the UV absorbance at 280 nm and corresponding fluorescence traces as specified in the chromatograms depicted in the supplementary file 3.

2.9 | Transmission electron microscopy

For TEM imaging of extracellular vesicles, Quantifoil (Großlobbichau, Germany) Cu 200 mesh R1.2/1.3 holy carbon grids were glow discharged for 60 s at -25 mA using a Bal-Tec (Balzers, Liechtenstein) SCD005 glow discharger and loaded into a Leica GP (Leica Microsystems) grid plunger. The climate chamber settings were 4°C and 75% relative humidity. Aliquots of 4 µl sample were applied to the carbon side of the grid and front-side blotted for 1–4 s using the instrument's sensor function and Whatman filter paper #1 (Little Chalfont, Great Britain). Instant vitrification was achieved by plunge-freezing grids into liquid ethane at approximately -180°C. Cryo-samples were imaged with a Glacios cryo-transmission electron microscope (Thermo Scientific, Hillsboro, OR, USA) equipped with a X-FEG and a Falcon3 direct electron detector (4096 × 4096 pixels). Digital images were recorded in low-dose mode using the SerialEM software (Mastrorarde, 2005) with defocus values of -8 µm at a magnification of 28,000x resulting in a pixel size of 5.2 Å.

For TEM imaging of cationic liposomes and siRNA- LNPs, 3.5 µl of LNPs were applied to freshly plasma-cleaned TEM grids (Quantifoil (Großlobbichau, Germany), Cu, 200 mesh, R2/1) and vitrified into liquid ethane using Thermo Scientific (MA, USA) Vitrobot Mark IV (18°C, 100% rel. humidity, 30 s waiting time, 4 s blotting time). The grids were subsequently mounted to the autogrid cartridges and loaded to Talos Arctica (Thermo Scientific, MA, USA) TEM. The microscope was operated at 200 kV. The cryo-TEM micrographs were collected using Falcon3 direct electron detection camera at 73,000x nominal magnification with the under focus in the range 3–10 µm and the overall dose of < 20 e/Å².

For TEM imaging of SiO₂ NPs, particles with and without protein label were applied to a formvar-coated copper grid (Science Services, Munich, Germany), air dried and measured utilising the LEO 912AB (Zeiss, Oberkochen, Germany) operated at 120 kV recorded with a Tröndle TRS Sharp Eye bottom-mounted 2 K CCD camera (Tröndle), filtered at zero energy loss and the recording was controlled by iTEM 5.0 software.

2.10 | Fluorescence correlation spectroscopy

Extracellular vesicle samples were analysed by FCS as described in detail in (Corso et al., 2019). Briefly, samples were measured on a Clarina II Reader (Evotec Technologies) with 488 nm argon ion laser excitation, a 40x water immersion 1.15 N.A. objective (UAPO Olympus), 50 micrometre pinhole and a SPCM-AQR-13FC avalanche photodiode (Perkin-Elmer Optoelectronics). The confocal volume was calculated in approximation according to (Lakowicz, 1999) using the measured diffusional correlation time t_{diff} of free dye (Alexa488, Life Technologies), the known translational diffusion coefficient of Alexa488 (Molecular Probes; $D = 280 \text{ mm}^2/\text{s}$) and the axis ratio fitted from calibration measurements. For each sample, several dilutions were made and measured in a 96-well glass bottom plate (Whatman) with 30 repetitive measurements of 10 s each. NP40s at 1% v/v (Nonidet P40 substitute, G-Biosciences) was used to induce vesicle disruption for determination of detergent sensitivity and quantification of GFP molecules per vesicle. Upon vesicle lysis (verified by a drop in the translational diffusion time), the number of diffusing GFP molecules increases according to the loading stoichiometry, whereas the brightness per particle decreases. Average numbers of molecules per vesicle were derived both, from the relative increase in particle numbers as well as the relative decrease in single particle brightness after correction for quenching of the fluorophore within the vesicles.

2.11 | HPLC-MS proteomics

EV samples corresponding to 20 µg of protein were lyophilized and reconstituted in 50 µl of lysis buffer (5.0% sodium dodecyl sulphate (Sigma-Aldrich, MO, USA), 50 mmol/L triethyl ammonium bicarbonate (pH 7.5; Sigma-Aldrich, MO, USA)). Proteins

were purified by S-trap micro columns (Protifi, Huntington, NY, USA) as described in detail earlier (Wolf et al., 2022). Tryptic digestion was performed at 47°C for 1 h. Purified peptides obtained from individual HEK293T EV-preparations were additionally labelled by tandem mass tags (TMT¹⁰129CTM, TMT¹⁰130CTM, and TMT¹⁰131CTM) included in the TMT 10 plex kit (Thermo Fisher Scientific, MA, USA). Peptides obtained from bovine milk Evs were measured directly without prior labelling.

Purified peptides were separated on a nano high performance liquid chromatography (HPLC) instrument (UltiMateTM U3000 RSLCnano, Thermo Fisher Scientific, Germering, Germany) equipped with an AcclaimTM PepMapTM 100 C18 column (500 mm × 75 μm i.d., 3.0 μm particle size, Thermo Fisher Scientific, Sunnyvale, CA, USA). The flow rate of the Nano-pump was set to 300 nl/min and the column oven temperature to 50°C. In all cases, 1.0 μl of sample corresponding to 2.0 μg of peptides were injected in microliter pick-up mode in technical triplicates. For HEK293T Evs, a multi-step linear gradient of mobile phase solutions A (H₂O + 0.10% formic acid) and B (acetonitrile + 0.10% formic acid) was applied as follows: 1.0% B for 10 min, 1.0–22.0% B in 290 min, 22.0–40.0% B in 110 min, 40.0–90.0% B in 20 min, 90.0% B for 20 min, and 1.0% B for 50 min. Peptides obtained from bovine milk Evs were separated with the following gradient program: 1.0% B for 10 min, 1.0–22.0% B in 100 min, 22.0–40.0% B in 25 min, 40.0–90.0% B in 5 min, 90.0% B for 20 min, and 1.0% B for 40 min.

MS data was acquired on a Quadrupole-Orbitrap[®] hybrid mass spectrometer (Thermo ScientificTM QexactiveTM Plus benchtop quadrupole-Orbitrap[®] mass spectrometer) hyphenated to the HPLC instrument by a Nanospray FlexTM ion source (both from Thermo Fisher Scientific, Bremen, Germany). The source was equipped with a SilicaTipTM emitter with 360 μm o.d., 20 μm i.d., and a tip i.d. of 10 μm (New Objective, Woburn, MA, USA). The instrument settings of the mass spectrometer are stated in detail in Eckhard et al. (2020). Selected parameters were optimised depending on the sample type: resolution of MS² scans was set to 35,000 or 17,500 and normalised collision energy to 32.0 or 30.0 for TMT-labelled and non-labelled peptides, respectively. The mass spectrometer was calibrated employing PierceTM LTQ Velos ESI Positive Ion Calibration Solution (Thermo Fisher Scientific).

MS peptide data were evaluated using MaxQuant 1.6.12.0 (Cox & Mann, 2008) employing default settings. For protein identification, two individual protein lists were obtained from the UniProt database. For HEK293T Evs, Swiss-Prot entries for *homo sapiens* were considered (access: 30.03.2020). Bovine milk Evs were evaluated using the reference proteome UP000009136 for *bos taurus* including both Swiss-Prot as well as TrEMBL entries (access: 12.05.2020). Decoy hits and contaminant protein identification were removed prior to log₁₀ transformation and subtraction of the median. Perseus 1.6.12.0 (Tyanova et al., 2016) and Instant Clue 0.5.3 (Nolte et al., 2018) were used for data processing and visualisations.

Mass spectrometry raw data are available at <https://doi.org/10.5281/zenodo.6587909>. Additionally experimental evidence for the identification of EV markers including human and bovine CD9, CD63, CD81 and TSG101 is provided in Supplementary File 6.

2.12 | EV immobilization and immunostaining

A detailed standard operating procedure (SOP) for immobilisation and immunostaining as well as a step-by-step optimisation of the protocol can be found in Supplementary File 4.

2.13 | Post isolation EV labelling

For DiI labelling, 35 μl of 1 × 10⁹ particles/ml of UF-SEC purified FP-tagged HEK293T Evs (CD63 mNeon stable line) were immobilised and formaldehyde-fixed on regular quartz glass (QG) slides following the immobilisation SOP (Supplementary File 4) provided in this manuscript. The slide was incubated with DiI (Fisher Scientific, MA, USA), diluted 1:1000 in PBS for 1 h followed by three washing steps with PBS and embedding in Vectashield embedding media (Vector Laboratories, CA, USA).

For Cy5-NHS ester labelling, 1 ml of 6 × 10¹¹ particles/ml of FP-tagged HEK293T Evs (CD63 mNeon stable line), isolated as described above, were incubated with 10 μM Cy5-NHS ester (Lumiprobe (Germany) CAS No.: 1263093-76-0) for 1 h at 37°C shaking with 1500 rpm. To remove free dye, the sample was purified by FPLC-SEC on a Superdex 20 Increase 10/30 GL column (GE Healthcare) as described above. The flow through was monitored by tracking the mNeon (504/517 nm) and the Cy5 (646/662 nm) fluorescence. Pooled EV fractions were concentrated to 200 μl with a 10 kDa MWCO Amicon Ultra 4 ml centrifugal filter. Particle concentrations and size distributions were determined by NTA.

For MemGlow labelling, 1 × 10⁹ particles/ml of UF SEC purified FP-tagged HEK293T Evs (CD63 mNeon stable line) were immobilised and formaldehyde-fixed on regular QG slides following the staining SOP (Supplementary File 4) provided in this manuscript. The slide was incubated with 200 nM of MemGlow (Hölzel Biotech, Germany) diluted in PBS for 1 h followed by three washing steps to remove excess dye and embedding in Vectashield embedding medium.

2.14 | Cell uptake assay

Human epithelial lung carcinoma cells (A549), kindly provided by the group of Prof. Dr. A. Risch (Paris Lodron University Salzburg, Austria) were cultured in F-12K Nut Mix medium (Gibco, MD, USA) supplemented with 10% FBS (Gibco, MD, USA) and 1% of a 100x antibiotic/antimycotic solution (Gibco, MD, USA), and cultured at 37°C, 5% CO₂ and 90% relative humidity over-night. 4×10^4 cells/ml were seeded in a 96-well μ -plate (Ibidi (WI, USA); 300 μ l/well) precoated with 20 μ g/ml Fibronectin-human plasma (Sigma Aldrich, MO, USA) diluted in PBS for 1 h. The next day the medium was changed to medium containing different concentrations (determined by NTA) of fluorescently labelled Evs as indicated. After 1 h the cells are washed once with medium and then fixed with Pen-Fix (Thermo Scientific, MA, USA) supplemented with 0.1 μ g/ml Höchst for 20 min and subsequently washed with PBS, pH 7.4 (Gibco, MD, USA) for three times. Fixed cells were kept in PBS in sealed plates and stored at 4°C.

2.15 | Formulation of Lipid- based nanoparticles (LNPs) and QC

Cholesterol and HEPES were purchased from Sigma-Aldrich. 1,2-dioleoyl-sn-glycero-3-phosphoethanolamine (DOPE) and 1,2-dioleoyl-sn-glycero-3-phosphoethanolamine-N-(Cyanine 5) (Cy5-DOPE) were purchased from Avanti Polar Lipids (AL, USA). AllStars negative Control siRNA labelled with AlexaFluor 488 was purchased from Qiagen (Germany). *N',N'*-Dioctadecyl-*N*-4,8-diaza-10-aminodecanoylglycine amide (DODAG) and cholesteryl-PEG³⁵⁰-aminoxy (CPA) lipid were synthesised as described in previously published studies (Kolli et al., 2015; Mével et al., 2010).

DODAG, cholesterol and CPA were dissolved in absolute ethanol, DOPE was dissolved in dichloromethane (all at 10 mg/ml) and Cy5-DOPE was dissolved in chloroform (1 mg/ml). Appropriate aliquots of these lipid stock solutions were mixed in the ratio DODAG/DOPE/cholesterol/CPA/Cy5-DOPE 20:49.5:20:10:0.5 (m/m/m/m/m) then heated up to 60°C. This lipid mixture was then injected into a 7-fold volume of 4 mM HEPES, pH 7, heated up to 60°C shaken manually and hard-vortexed for 5 min. The organic solvents were first evaporated in a water bath (at 65°C) for 30 min and then slowly evaporated using an Eppendorf Vacufuge Concentrator (at 60°C) for 10 min. The resulting suspension of fluorescent labelled cationic liposomes free of organic solvents were extruded using Avanti® Mini-Extruder through one Whatman® Nucleopore™ polycarbonate membrane (pore size 100 nm) with 14 extrusion cycles at room temperature and collected in the 15th extrusion cycle to yield fluorescent labelled empty LNPs. Under sterile conditions, aliquots of an siRNA stock solution (50 μ M) were then added gradually (10 additions of the same volume) to the fluorescent-labelled empty LNPs up to a final mol charge ratio of 6:1 m/m (ratio of positive charges of cationic lipids to negative charges of siRNAs). After the addition of each aliquot, the mixture was gently agitated by vortex mixing for 15 s, and finally the resulting fluorescent-labelled siRNA-loaded LNPs were incubated for 30 min at room temperature before further studies.

Fluorescent-labelled empty and siRNA-loaded LNPs were separately characterised to verify their physicochemical properties. Particle size distributions were obtained by NTA as described for Evs, using a Nanosight LM14C equipped with a 488 nm laser and with NTA 2.3 analytical software. The samples were diluted in 4 mM HEPES, pH 7, and three videos (1 min each) were recorded with a camera level of 13 and a detection threshold of 5. These data were further validated using dynamic/electrophoretic light scattering (Zetasizer Nano ZS, Malvern Panalytical, UK) by which size distributions, polydispersity index (PDI) and ζ -potentials were analysed. Size and PDI measurements were performed at 25°C in 4 mM HEPES, pH 7, with 15 runs (5 s each) per measurement. Z-potential was measured in DTS1070 capillary cells at 25°C with the automatic measurement duration setup and the samples being diluted in 4 mM HEPES, pH 7.

2.16 | Mesoporous silica nanoparticle (NP) preparation and QC

Mesoporous silica nanoparticles (SiO₂ NPs) were synthesised and characterised as previously reported by Mills-Goodlet et al. (2021). Briefly, tetraethyl orthosilicate (TEOS) was used as the silica source and the pores were introduced using cetyltrimethylammonium bromide (CTAB). The silica content in the nanoparticle aqueous suspension was quantified using the silicomolybdic assay. The pore size and primary size of SiO₂ NPs were measured by high-resolution transmission electron microscopy as described in Section 2.9. Furthermore, the hydrodynamic size and zeta potential of the synthesised particles were determined by NTA as described for Evs but using a NanoSight LM10 instrument (Malvern Panalytical, Malvern, United Kingdom) and a ZetaSizer Nano ZS system (Malvern Panalytical, Malvern, United Kingdom), respectively.

2.17 | Fluorescent protein labelling

β -Lactoglobulin from bovine milk (Cat: L3908, Sigma-Aldrich, St-Louis, USA) and lysozyme from chicken egg white (Cat: L4919, Sigma-Aldrich) were used as model proteins for NP loading displaying different isoelectric points which can result in different binding efficiencies. Initially, the proteins were labelled with the NHS-reactive fluorophores (β -lactoglobulin with TMR-NHS (Lumiprobe, Germany) and lysozyme with Cy7-NHS (Lumiprobe, Germany) where 1 mg of each protein was incubated with a 10-fold molar excess of the fluorophore in a shaker for 1.5 h at room temperature (total reaction volume of 500 μ l 0.1 M NaHCO₃ buffer; pH 8.8). Unreacted dye was removed by gel filtration using the Cytiva NAP-5 column (Cat: GE17-0853, Sigma-Aldrich) and 5 mM sodium phosphate buffer pH 7.4 as eluent. The amount of protein in the fractions was semi-quantitatively determined by SDS-PAGE using the ImageLab Software 6.0.1-based on the standard concentrations of pure proteins (unlabelled).

2.18 | Quantification of labelled protein concentrations by reverse phase-HPLC

For quantification of β -lactoglobulin and lysozyme and for determination of labelling efficiency, reversed-phase (RP)-HPLC was performed on a Shimadzu Prominence RP-HPLC system equipped with a SPD-M20A Photodiode Array Detector (Shimadzu, Japan) and a RF-20A Fluorescence Detector (Shimadzu, Japan). Each sample was injected in triplicates (injection volume 10 μ l) on a C18 column (C18 250 \times 4.6 mm, 5 μ m; AnalyticShop) and eluted in a binary gradient of H₂O:TFA 99.9:0.1 v/v (Mobile Phase A) and CH₃CN:TFA 99.9:0.1 v/v (Mobile phase B) at a flow of 0.5 ml/min at 40°C temperature. The gradient used, expressed in the concentration of the mobile phase B was: 0–2 min. – 0%; 2–10 min. – 90%; 10–15 min. – 90%; 15–17.5 min. – 0%; 17.5–20 min. – 0%. The UV-Vis absorbance at 280 nm from the DAD detection as well as fluorescence were recorded (dual wavelength mode: Ex./Em. 555/580 nm for TMR and 750/773 nm for Cy7; the detector sensitivity was set to medium).

2.19 | Loading of SiO₂ NPs with labelled proteins

The labelled proteins were individually bound to NPs by incubating 1 mg/ml of SiO₂ NPs with 0.05 mg/ml of lysozyme-Cy7 and 0.1 mg/ml of β -lactoglobulin-TMR in water for 17 h at 4°C on a rotator. Furthermore, for combined loading of both proteins to the NP surface, similar incubation steps were followed with simultaneous incubation of the particles with both proteins (lysozyme-Cy7 at 0.025 mg/ml and β -lactoglobulin-TMR at 0.5 mg/ml). The loaded NP samples were then centrifuged at 14000 g for 1.5 h to separate the NPs (pellet) from unbound proteins (supernatant). The amount of protein conjugated to SiO₂ NPs was then qualitatively and quantitatively determined from the supernatant and pellet using SDS-PAGE and RP-HPLC.

2.20 | Widefield fluorescence microscopy

Cellular and single vesicle imaging were performed on Olympus IX73 or IX83 microscopes. The IX73 microscope was equipped with a Lumencor Sola SMII excitation source and spectral filter cubes for DAPI (AHF-LED-DAPI-385 filter set), GFP (ET470/40x excitation filter, dichroic mirror T495LP and ET525/50 m emission filter), Cy3 (ET545/25x excitation filter, T565LP dichroic mirror and ET605/70 emission filter) and Cy5 (ET620/60x excitation filter, T660LPCR dichroic mirror and ET700/75 m emission filter) measurements. For cell imaging during transfection experiments a 10x (Olympus CACHN10XIPC-1-7/0.25 achromat objective) or a 20x objective (Olympus PLCN20XPH-1-7/0.4 plan Achromat C objective) were used, single vesicle imaging was performed using a 100x oil objective (UPLXAPO100XO NA1.45).

The IX83 microscope was equipped with spectral filters for DAPI, GFP, Cy3, Cy5 and Cy7 and five different objectives. For imaging of the cell uptake assay a 40x objective (UPLXAPO40X NA 0.95) and a Hardware autofocus (IX3-ZDC2-830 Z Drift Kompensation) enabling automated plate scanning were used. For single vesicle imaging a 100x oil objective (UPLXAPO100XO NA1.45) was used. A SPECX7IR-LFIB Light Engine (Lumencor) was used as excitation light source with six LEDs and additional excitation filters for the following wavelengths: 395/25 nm, 438/29 nm, 475/28 nm, 555/28 nm, 575/25 nm, 635/22 nm and 730/40 nm. Either a Penta-Band dichroic mirror (AHF-SPX-PSEM) or specific emission filter cubes for the respective fluorophores were used in the optical path (49002—ET—EGFP filter cube: ET470/40x EX and ET525/50 m EM; 49004—ET—CY3/TRITC filter cube: ET545/25x EX and ET605/70 m EM).

2.21 | Super resolution microscopy

To obtain sub-diffraction limit resolution images of single Evs, 1×10^9 Evs in 1 μ l were stained with a 'tetramix' of anti-CD9, (R&D Systems, USA), anti-CD63, (Becton Dickinson, USA) and anti- CD81 (R&D Systems, USA), all conjugated to AlexaFluor 647

(Gomes et al., 2022) or with antibodies supplied in the EV profiler Kit (Oxford Nanoimaging, UK) including anti-CD9-ATTO488, anti-CD63-Cy3 and anti-CD81-AlexaFluor647. Samples were processed according to manufacturer's instructions to immobilise the stained EVs on the chips provided with the ONI EV profiler kit. Three fields of view were recorded for each sample using direct stochastic optical reconstruction microscopy (dSTORM) on a Nanoimager S Instrument (Oxford Nanoimaging, UK) using 40%, 20% and 20% power for the 488 nm, 561 nm and 640 nm laser, respectively. For localisation mapping, 2500 images were recorded per channel. To quantify the images and to detect colocalisations, we either used the EVAnalyzer software as described in the manuscript, or the CODI platform (Oxford Nanoimaging, UK) as described previously (Wolf et al., 2022).

2.22 | Image processing by EVAnalyzer

Image analysis was performed with Fiji and the EVAnalyzer plugin (version 7.2.1) downloaded on a 64-bit operating system with 8 GB RAM and an Intel quad Core™ i5-8265U CPU @ 1.60 GHz. The images are saved as Olympus 'vsi' format, however, also tif, jpg, ics and czi formats are supported by the EVAnalyzer. 16bit grayscale images with 2048 × 2048 pixels (IX83) or 1920 × 1200 pixels (IX73) resolution were used.

The image analysis processing is described in detail in Supplementary File 1 and 2 (Handbook). Briefly, all images selected for the analysis with EVAnalyzer belonging to the same experiment are compiled into one input folder and sorted into subfolders according to the experimental design. EVAnalyzer processes all images within the selected input folder with the same settings and stores the results by default into an automatically generated output folder. The results include a report file in .xlsx format (compatible with Microsoft Excel 2007 and newer or other related spreadsheet programs like OpenOffice Calc), output images and a .json file (contains all settings and can be used to reload settings). The report file is organised according to the subfolder structure in the input folder. Within one experiment all samples and controls are analysed with the same settings.

For single channel images analysed by the 'EV Count' pipeline, the Series import 'series 2' was used. For all multichannel images 'series 1' was used. To find the appropriate image series, a test image was opened in Fiji, which offers different Bio- Formats Input Series Options. The different image types were assigned to individual channels whereas C = 0 corresponds to the first channel recorded. Different image types can be either channels with EVs (EV_DAPI, EV_GFP, EV_CY3, EV_CY5, EV_CY7, EV_CY3FCY5), with cells (CELL_BRIGHTFIELD, CELL_FLUORESCENCE), with nuclei, negative control, background or a Tetraspeck (TS) beads channel. A maximum of five channels can be analysed in version 7.2.1, however, this may be expanded in future releases.

For single EV imaging either the function 'EVCount' or 'EVColoc' was used with 1–3 individual channels. In all automated 'single vesicle imaging' analysis (except for Figure 2e) a constant threshold (TH) was set by the user to assure comparability between the analysed images. The threshold was chosen by using the preview option integrated in the EVAnalyzer. Additionally, the output generated by the EVAnalyzer was compared to the original images for quality control to assure that an accurate TH was set. Within all analyses (except for Figure 2e) a size filter of 3–99999 pixels was set to remove small artefacts. More specific filtering is used in the following Figures:

In Figure 6d a colocalisation area of 70% was compared to the default setting of 1% colocalisation. The analysis performed for Figure 9hk used spike-in of Tetraspeck beads for focusing. Accordingly, one channel was specified as 'TETRASPECK_BEAD' to exclude spots colocalising with TS-beads from the EV detection.

For Figure 2e the images were either processed by manual quantification or with the EVAnalyzer plugin. For manual quantification an image was manually opened in Fiji, followed by manual TH adjustment (Path: Image/Adjust/Threshold/Apply), particle analysis (Path: Analyze/Analyze Particles). Size and circularity filters were set to 'off' (Size: 0-Infinity; Circularity 0–1). A summary of the data was transferred to an Excel list and the same was repeated for all 10 images. For quantification in the EVAnalyzer pipeline either an auto threshold was set (Max Entropy, Moments, Otsu, Triangle, Li, Min Error) or a defined TH was chosen by each user and adjusted in the preview images. No size or circularity filters were used. With the EVAnalyzer, all 10 images were automatically analysed in a sequence and a report output file was automatically generated.

For EV quantification in the cell the pipeline 'EVCount per Cell- remove cropped cells' was used. 'Series 1' was used for import. The four different channels were specified as EV_GFP (CD63mNeon expressing HEK293T EVs), EV_CY5 (CY5 NHS label), CELL_BRIGHTFIELD and NUCLEUS (Höchst stained nucleus). EVs were detected with a user defined constant TH. Cells were detected with the automated MinError threshold and the nuclei were detected with the automated Triangle threshold. A z-projection of the individual z-stacks was done before image processing ('Z-Projection' was set to 'max' for all used channels). For EV detection a size filter of 3–99999 was used. All 336 images (16 images/well; three wells per condition; seven conditions) were processed in a batch using the same settings.

3 | RESULTS

3.1 | EVAnalyzer is a new open-source plugin for Fiji, developed for automated single vesicle quantification from fluorescence microscopy images

A robust, straightforward process for routine characterisation of EVs at the single vesicle level by fluorescence imaging requires essentially three steps (Figure 1a):

1. Immobilisation of EVs on optical surfaces for fluorescent detection by different strategies including immunolabelling, detection of intrinsic fluorescence of FP-tagged EV markers, chemical labelling or loading with fluorescent cargo.
2. Fluorescence imaging, which can range from standard widefield, to confocal or more advanced super-resolution imaging technologies.
3. Image analysis, which should ideally enable automated, quantitative analysis by batch processing of multiple images.

Here we describe the development of a robust procedure for EV sample preparation, fluorescence imaging as well as image analysis using exclusively standard laboratory equipment and a new open-source plugin for Fiji, which we are making publicly available under the name EVAnalyzer. The plugin was developed in the open-source code editor *Visual Studio Code*, compiled in Java and offers image processing tools optimised for both, single vesicle quantification in purified and complex EV samples, as well as quantification of cell uptake data at the single cell–single vesicle level. EVAnalyzer has been designed for fast and automated quantification of multiple images in a batch process and can be downloaded via the Fiji repository (version 7.2.1) or via GitHub (<https://github.com/joda01/evanalyzer/releases>). To enable further community development, the source code is provided together with a docker image comprising all tools and libraries to compile the plugin.

The software development and the detailed image processing procedures are described in Supplementary File 1. A handbook is provided in Supplementary File 3. An outline of the plugin workflow is shown in Figure 1b. Essentially, the software has been organised into four packages (I) Filters: classes and methods for image processing algorithms. To minimise the processing time, an image abstraction is used for multi-threading. (II) Pipelines: This package comprises pipelines to automate the succession of image processing steps for different applications. In the current version (7.2.1), EVAnalyzer provides default pipelines for vesicle detection in single and multiple channels, multi-channel colocalisation as well as single vesicle–single cell quantification for cellular uptake assays and high content screening applications. The identified vesicles are annotated with their features such as brightness, circularity and area for each spectral channel and are quantified with or without additional filtering or classification (e.g., based on colocalization area or size thresholds). EVAnalyzer provides additional features to generally facilitate processing of large sets of images. This includes preview images to facilitate parameter setting, automated Z-stack processing (e.g., generation of maximum intensity projections) and corrections for chromatic aberrations. (III) Output: After batch processing of all images, an output file is generated with spreadsheet tables in .xlsx format providing mean values for each image, individual values for each single spot, hyperlinks to the processed images (output images) and the settings of the analysis. Additionally, a .json file is generated which can be read into EVAnalyzer for re-using previously applied settings. Package (IV) comprises the code for the EVAnalyzer control window (Graphical User Interface, GUI).

EVAnalyzer currently supports .tif, .vsi, .jpg, .ics and .czi file formats (8-bit and 16-bit). Theoretically, there is no limitation of the number of images that can be batch processed by the plugin, however, the data volume for a given session is practically limited by the available free RAM (typically ca. 10 MB of free RAM required per image). Details on typical processing times and data volumes are listed in the handbook (Supplementary File 2).

3.2 | Immobilisation and immunolabelling of EVs for imaging based single vesicle quantification using standard laboratory equipment

EVAnalyzer was first used to establish a robust, straightforward and reproducible process for immobilising, detecting and imaging EVs on regular microscope slides suitable for widefield (as well as confocal and super-resolution) fluorescence microscopy. The systematic development and optimisation of the process is described in detail in Supplementary File 4 and included testing of different commercially available surfaces, immobilisation conditions, fixatives, blocking agents, influence of detergents, embedding media and storage stability. EVs from HEK293T cells stably transfected with a CD63-mNeon transgene were used to monitor the vesicles throughout all steps. As a result, we provide an SOP with the optimised protocol using exclusively commercially available, low cost materials and reagents (Supplementary File 4). To test the robustness and reproducibility of this protocol, three independent operators followed this SOP for immunostaining of CD81- emGFP HEK293T EVs using an anti-CD81 antibody (Figure 2a). Independently obtained microscopy data were then analysed with EVAnalyzer by the same operator (operator

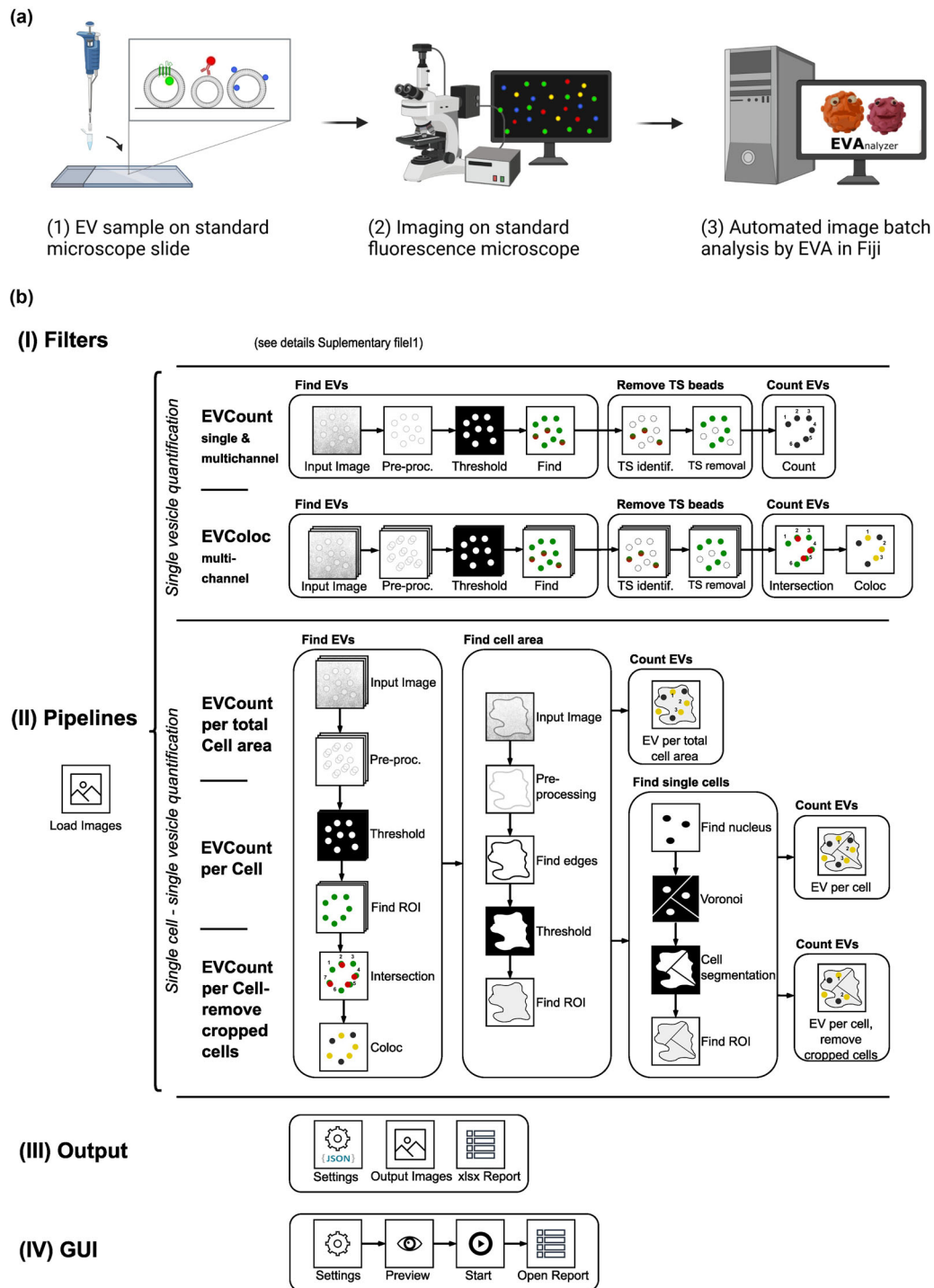


FIGURE 1 Quantitative single vesicle analysis by EVAlyzer. (a) General workflow for EV imaging by standard laboratory equipment. (b) The Fiji plugin EVAlyzer is organised in four packages comprising (I) Filters from the Fiji repository, which are described in more detail in Supplementary File 2 and (II) specifically developed pipelines for image processing which enable the quantification of EVs in vitro or in cells for diverse types of samples and applications. Pipelines for single vesicle quantification comprise options for single and multi-channel analysis ('EVCount') as well as colocalisation of detected particles across channels ('EVColoc'). To detect the vesicles ('Find EVs'), images are processed by the following steps: First, pre-processing for background subtraction using a rolling ball filter and, optionally, subtraction of a background image. Second, smoothing to blur residual noise using a Gaussian filter. This allows to reduce low intensity background noise. Third, an intensity threshold is defined (by the user or the software) to optimally discriminate between signal and noise. During this step, the image is converted into a binary image. Using the binary image, regions of interest (ROI) are converted into individual objects. Additional area and circularity filters can be applied by the user. If internal reference particles such as TetraSpeck (TS) beads or orthogonally labelled EVs are used, these can be excluded ('Remove TS'). Identified objects are quantified and annotated with their individual parameters including brightness, circularity, area and spectral channel. For colocalisation calculation ('EVColoc'), these preprocessing steps are performed for multiple channels (up to 5 channels in version 7.2.1). The regions of interests are then compared between two or more channels as defined by the user. Per default, the object is classified as colocalised

(Continues)

FIGURE 1 (Continued)

if the intersection of the ROI areas is > 0 . This can be individually changed with a min colocal factor or a snap area. Pipelines enabling single cell- single vesicle quantification essentially require EV detection ('Find EVs') and cell area detection ('Find cell area') and optionally can also include nuclei detection for single cell analysis ('Find single cells'). Package (III) comprises the code for generation of output files, images and documentation of the settings. The graphical user interface (GUI) is covered in package (IV). See details of all EVAnalyzer packages, filters and pipelines in Supplementary File 1 and the handbook in Supplementary File 2.

2) for total EV numbers and % colocalization, which led to almost identical results (Figure 2a-c), thereby demonstrating the robustness of the protocol.

To validate the image analysis output by EVAnalyzer, four independent operators with expertise in EV analytics were asked to analyse 10 images of CD63mNeon HEK293T EVs in a blinded manner with manual thresholding and counting in Fiji. These results were compared to automated batch processing of the same images by EVAnalyzer using either auto thresholding, or threshold setting by the four users (Figure 2e). As default we recommend setting a constant threshold for all images within a series, whether in EVAnalyzer or with manual image analysis. Depending on the application, however, automated threshold setting may be preferable. Based on our experience, Li and Triangle auto threshold filters work generally well on samples with low background, while MaxEntropy is superior for discrimination of bright spots from diffuse background. As illustrated by the example in Figure 2e, the optimal auto threshold settings depend on the application and should be tested on a subset of images by visual inspection of the recognized particles in the output images as compared to the original images prior to batch processing. Manual image analysis resulted in relatively comparable results between three out of four operators. One user, however, obtained substantially different results for two out of the 10 images, revealing the possible user bias by manual image analysis with subjective and image-to-image threshold setting. In contrast, the results of automated image batch processing by the same four operators using EVAnalyzer were highly consistent between the individual users and further corresponded well to the results of the manual image analysis by the majority of the operators. This confirms that automated image batch processing by EVAnalyzer provides results which are consistent with the average subjective classification of light diffraction limited spots as EVs by the human eye, though with substantially reduced processing time.

In the following examples we describe how EVAnalyzer can be applied to address a variety of common questions of high relevance for EV research, with an intention to illustrate the breadth of information that can be generated. Additionally, we also provide prototypic examples for synthetic nanoparticle analysis since we foresee a wide application potential also in nanomaterial sciences. For all applications described here, we have made an emphasis on straightforward implementation in virtually all laboratories with access to standard equipment and infrastructure. As exemplified for the single vesicle–single cell uptake assay, they can, however, also be miniaturised and automated for medium- to high-throughput screening for labs with access to automated imaging instrumentation. Pre-sets for single vesicle detection, colocalisation and cell uptake quantification are provided in the plugin as well as in the handbook (Supplementary File 2) as a starting point for other researchers using the plugin.

3.3 | EVAnalyzer can be applied for rapid quantification of EV subpopulations at the single vesicle level in purified and crude samples

In most EV research projects there is an increasing demand for characterising subpopulations at the single vesicle level in both, purified and crude EV samples. To exemplify this, we first used EVs from HEK293T cells genetically engineered with fluorescent protein tagged tetraspanins for in situ antibody validation. As illustrated in Figure 3a, immunostaining of FP tagged EVs from transiently transfected cells can result in different species: (i) tetraspanin-FP tagged EVs which are recognized by the antibody and resulting in a double positive vesicle (yellow, true positives), (ii) EVs with endogenous tetraspanins recognized by the antibody (red only, true positives), (iii) EVs with FP-tagged tetraspanins not recognized by the antibody (green only, false negatives) and (iv) unspecific binding of the antibody (red only, false positives). Ideally, all green fluorescent EVs should be recognized by the antibody. This can be assessed by the fraction of colocalisation (% red in green), which is a direct measure of antibody sensitivity. For red only vesicles it can per se not be discriminated what the contributions of true and false positives are. This requires additional controls such as genetic knockouts or combination with orthogonal, non-neutralising antibodies recognising the same antigen. Unspecific binding of the secondary antibody as well as antibody precipitates can be determined by corresponding controls omitting the primary antibody or samples without EVs. HEK293T EVs with CD63-mNeon, CD81-emGFP or CD9-emGFP were purified by UF-SEC (Figure 3b and Supplementary File 3) and subjected to immunostaining with their corresponding matched antibodies (anti-CD63, anti-CD81 or anti-CD9, respectively). EVAnalyzer was used to quantify the total numbers of EVs in both, the GFP/mNeon and the AlexaFluor555 channels, as well as the colocalisation between the two channels using the 'EVColoc' pipeline. As shown in Figure 3c and d, the CD63 antibody used in this example recognised over 80%, the two CD81 and CD9 antibodies even $> 90\%$ of all tetraspanin-FP positive EVs, demonstrating a high sensitivity. For CD9 and CD81, approximately 70% of all antibody positive vesicles lack the FP tagged transgene, which can largely be explained by the incomplete (transient) transfection of the parent cells (Supplementary File 3). In contrast, only a small fraction of red only

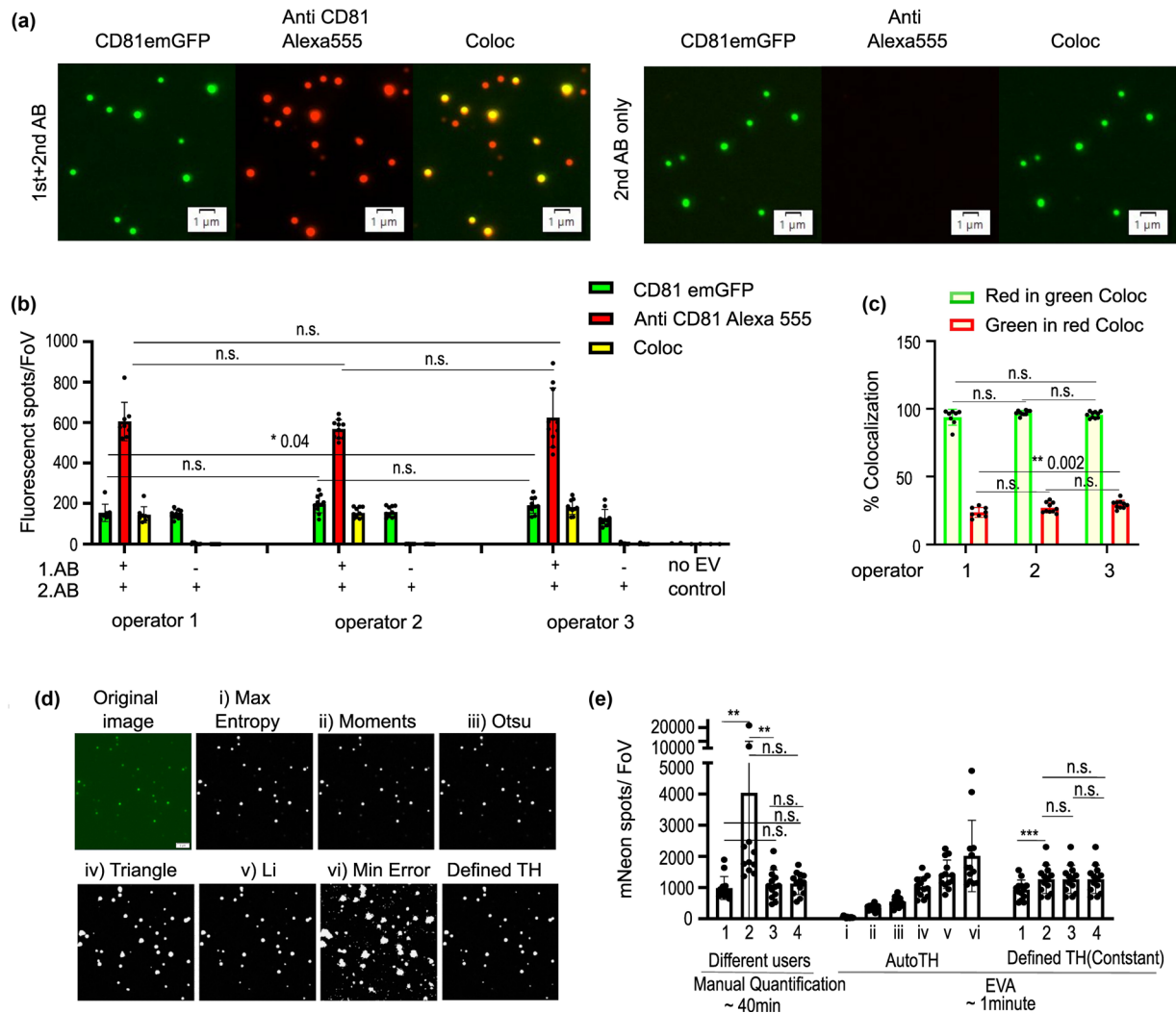


FIGURE 2 Operator variability of EV immobilisation and immunostaining SOP and validation of image analysis by EVAnalyzer. (a-c) Immunostaining of HEK293T CD81-emGFP EVs with anti-CD81 (AlexaFluor555) by three independent operators using the SOP provided in Supplementary file 4. (a) Representative images from operator 2 on vesicles incubated with first and secondary antibody (left) or without the first antibody (right) are shown in the top panel. (b) Fluorescent spot quantification in EVAnalyzer was performed with identical settings in the EVColoc pipeline. (c) % colocalisation red-in-green or green-in-red. Statistics: Man Whitney U Tests; n.s. non significant, * $p < 0.05$ for fluorescent spots/FoV and One Way Anova or Man Whitney U test for %Colocalisation. (d-e) Comparison of vesicle quantification (HEK293T CD63-mNeon EVs) by either manual quantification or EVAnalyzer by different operators. Manual quantification: Individual threshold setting by the user for each image in Image J. EVAnalyzer: each user defined a constant threshold facilitated by the EVAnalyzer preview option (notably, three out of the four users independently chose an identical TH). In addition different Auto-Thresholds were compared. The original image (green) as compared to thresholded images (white) are shown (d). The average processing time to obtain the results is shown on top. Green: mNeon fluorescence. Red: AlexaFluor555 fluorescence. Yellow: colocalisation. a.u.: arbitrary units (relative intensity from 16 bit grayscale image). All data represent averages and standard deviations of 10 individual images and are representative for one out of at least three independent experiments. Statistics: RM one way ANOVA for defined threshold testings of four individual users and Friedman test for manual quantification. n.s. non significant, ** $p < 0.01$, *** $p < 0.001$.

vesicles was detected by CD63 antibody staining of CD63-mNeon EVs. The lower abundance of non-mNeon positive vesicles detected by the CD63 antibody is well in line with the fact that these samples were derived from a stably transfected HEK293T cell line, whereas the CD9-emGFP and CD81-emGFP EVs were derived from transiently transfected cells. No unspecific binding of the secondary antibody was detected.

These data validate the immunostaining and image analysis process for highly enriched EV samples such as obtained by UF-SEC. Certain applications would, however, be greatly facilitated by analysis directly in conditioned medium (Figure 3b), thereby minimising the required sample preparation time and any potential bias introduced by the isolation principle. We therefore compared CD81 immunostaining on CD81-emGFP HEK293T EVs either isolated by UF-SEC or directly in conditioned medium (Figure 3c, bottom). The vesicles per FoV in CM samples were in the upper range (ca 3000 vesicles per FoV). This demonstrates that the surface capture also works directly in conditioned medium, and that the EV concentration in CM is in a suitable

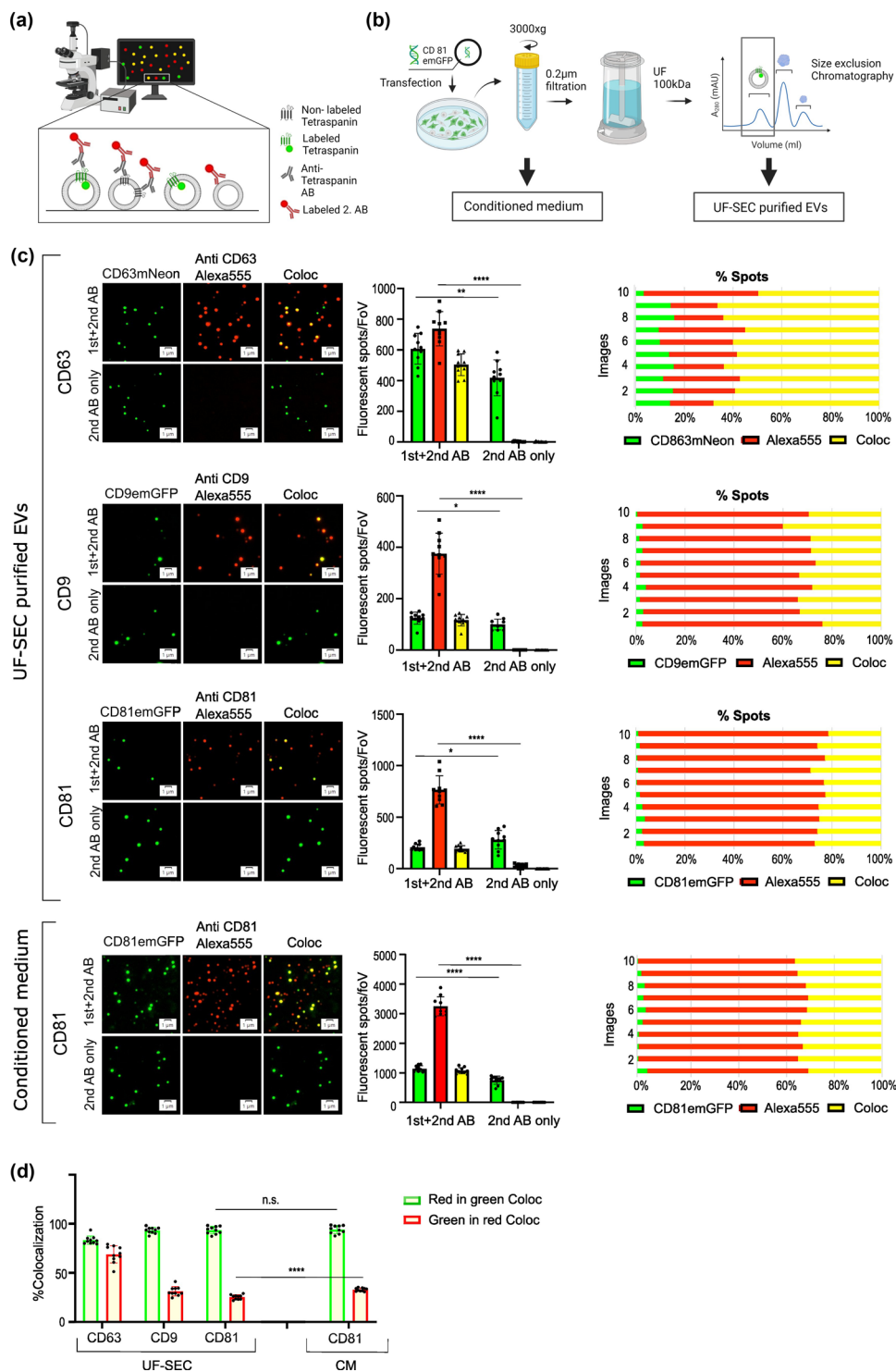


FIGURE 3 Single vesicle imaging-based antibody validation. (a) Cartoon representing the possible species obtained for anti-tetraspanin antibody staining of EVs engineered to express fluorescent protein tagged tetraspanins. (b) General workflow for EV isolation by UF-SEC exemplified for CD81-emGFP tagged EVs. (c) UF-SEC enriched EVs from HEK293T cells transfected with CD81-emGFP, CD9-emGFP or stably expressing CD63-mNeon were immunostained with their corresponding antibodies with detection by a secondary antibody labelled with AlexaFluor555. Controls without the primary antibody were used to determine unspecific binding of the secondary antibody. For each tetraspanin, representative images of immune stained samples are shown in the left panel. Middle panel: Total number of fluorescent spots per FoV in the GFP/mNeon (green) and AlexaFluor555 channels (red), as well as number of double-positive spots (Coloc, yellow). Right panel: Percentage of green only, red only and double positive spots for each individual FoV. Anti-CD81 immunolabelling of CD81-emGFP EVs sampled directly from conditioned medium is additionally shown in the bottom panel. Statistics: Unpaired t test (CD63 green spots, CD81), Welch's t test (CD63 red spots) Mann Whitney test (CD9, CD81, CD81 CM); n.s. Non significant, * $p < 0.05$, ** $p < 0.01$, *** $p < 0.001$, **** $p < 0.0001$. (d) % colocalization of particles detected by the antibody (AlexaFluor555) per GFP/mNeon positive particles (red in green) and of GFP/mNeon positive particles per AlexaFluor555 positive particles (green in red) is shown for all samples. Green: mNeon/GFP fluorescence. Red: AlexaFluor555

(Continues)

FIGURE 3 (Continued)

fluorescence. Yellow: colocalization. Statistics: Unpaired t test, n.s. Non significant, ****p < 0.0001. All results were generated using the EVColoc pipeline with defined thresholds constant within the image series for each graph. Data represent averages and standard deviations of 10 individual images and are representative for one out of at least three independent experiments.

range without any enrichment for direct application of our SOP, at least for EVs derived from HEK293T cells. Remarkably, the relative quantification data were almost identical for CD81-emGFP EVs from CM and after UF-SEC, demonstrating that the immunolabelling with single vesicle quantification can be directly applied in crude samples such as conditioned medium.

3.4 | Single vesicle brightness analysis by EVAnalyzer provides information on molecular loading densities and vesicle subpopulations

EVAnalyzer not only counts but also annotates each vesicle with its additional parameters such as intensity, circularity or area in all channels. Therefore, a multidimensional analysis with cross-correlation at the single vesicle level is possible—in analogy to flow cytometry or high content screening technologies. We would like to point out that widefield imaging cannot resolve sizes beyond the light diffraction limit. On our microscope using the $100\times 1.45\text{NA}$ objective the Abbe's resolution limit is in the range of 200–400 nm, depending on the wavelength. For objects smaller than the resolution limit, the apparent spot size becomes primarily a function of the fluorescence brightness of the point light source and should not be misinterpreted as true EV size. To derive total intensities for each vesicle, the mean intensity was multiplied with the spot area, resulting in the 'sum intensity per particle'. We next tested how well the vesicle brightness obtained by fluorescence imaging correlates with the number of fluorescent molecules per vesicle. We used EVs from HEK293T cells engineered to express different versions of FP-tagged CD63. This included stable, random integration of CD63-mNeon (Wiklander et al., 2019) or CD63-GFP ('OE', (Strohmeier et al., 2021)), as well as transient transfection of CD63-emGFP. In addition, we used a HEK293T line with GFP engineered into the CD63 locus by CRISPR/Cas9 technology ('CD63-GFP CRISPR') (Strohmeier et al., 2021). EVs from these different parent cells were isolated by UF-SEC (Supplementary File 3) and analysed by Fluorescence Correlation Spectroscopy (FCS) to determine the average number of fluorescent molecules per vesicle, following a previously described protocol (Corso et al., 2019). For the four different EV samples, the loading densities of CD63-FP ranged from ca 30 molecules/vesicle for the CD63-mNeon stable line, to 2–3 molecules/vesicle for EVs from CD63-GFP CRISPR cells (Figure 4a). These samples were then imaged by fluorescence microscopy with quantification using the 'EVCount' pipeline of EVAnalyzer (constant threshold setting) to derive sum intensities per vesicle as explained above. As shown in Figure 4b, the mean of the sum intensity per vesicle correlated well with the number of molecules per vesicle, indicating that single vesicle brightness analysis allows to estimate and compare molecular loading densities. Figure 4c illustrates the additional information provided by analysis of single vesicle brightness distribution, revealing the heterogeneity across the sample and the potential presence of defined subpopulations.

3.5 | Application of EVAnalyzer for rapid optimisation of genetic EV engineering directly in conditioned medium

Much EV research builds on genetically engineered EVs, such as for tracking EVs with fluorescent reporters (Sung et al., 2015; Verweij et al., 2018) or the development of modified EVs as therapeutics (Claridge et al., 2021; Dooley et al., 2021; Gupta et al., 2021; Wiklander et al., 2019). Monitoring secreted EV populations directly in small volumes ($35\ \mu\text{l}$ or below) of conditioned medium provides an opportunity to rapidly optimise genetic engineering of EVs, exemplified in some simple prototypic applications shown in Figure 5. We transiently transfected expression constructs for fluorescently tagged tetraspanins in HEK293T cells under different conditions and monitored both, the parent cells as well as the secreted EVs by quantitative single vesicle imaging after immunostaining directly in conditioned medium. Interestingly, at low polyethyleneimine (PEI) and plasmid concentrations, the transfection resulted in an approximately 4-fold increase in the total number of CD63 positive vesicles detected in conditioned medium (Figure 5a,b). This is consistent with previous notions that cells generally secrete more exosomes upon stress (e.g., Essandoh et al., 2015; Qin et al., 2021). At increasing concentrations of plasmid /PEI, the total number of CD63 positive vesicles declined again, in line with an apparent cell growth inhibition at elevated transfection stress (Supplementary Figure 1a). As expected, the fraction of CD63-emGFP positive vesicles increased with the PEI/plasmid concentration (Figure 5b, d (Green in red coloc)), while the absolute numbers of vesicles carrying the transgenic CD63 remained relatively constant above ca $4\ \mu\text{g}$ plasmid (Figure 5c). This indicates that increasing levels of CD63-emGFP in the parent cells increase the fraction but not the total number of CD63 positive vesicles, whereas mild cellular stress generally boosts EV secretion.

In-depth single vesicle brightness analysis revealed that the mean intensity of CD63 antibody staining increased with the transfection dose of CD63-emGFP plasmid (Figure 5e). In contrast, the average brightness of CD63-emGFP per GFP positive

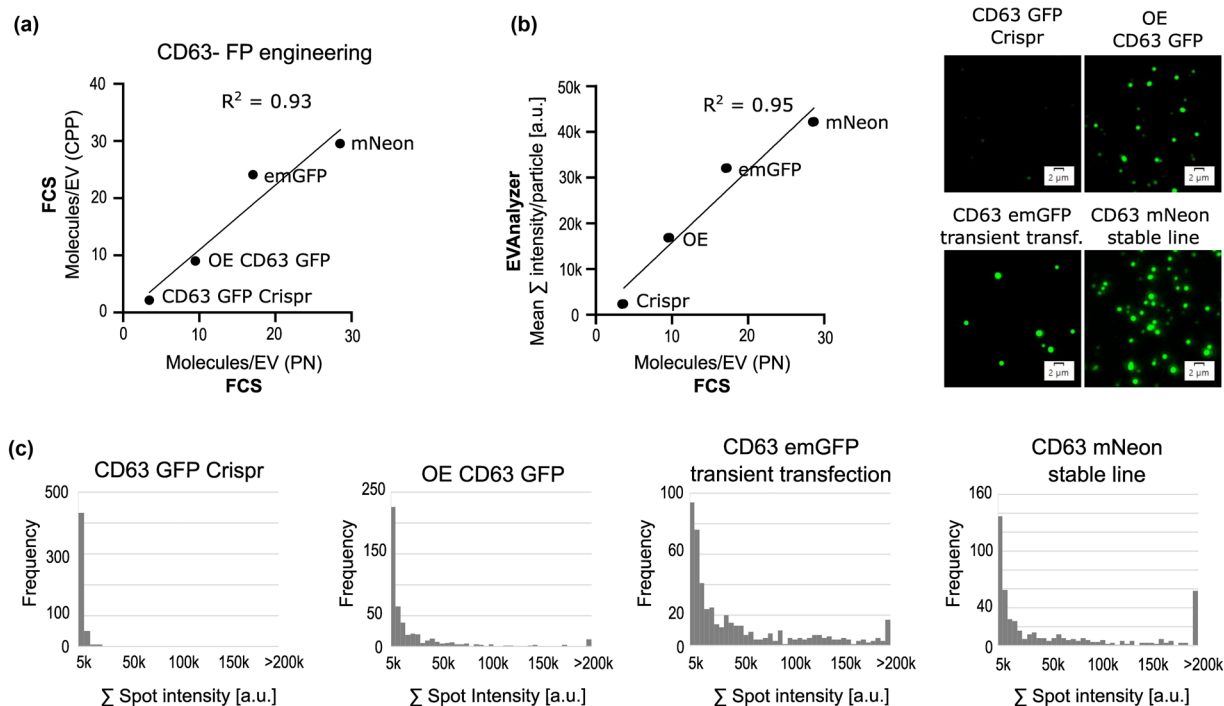


FIGURE 4 Single vesicle brightness analysis by EVAnalyzer. (a) UF-SEC purified EVs from HEK293T cells engineered with different CD63-FP expression constructs were analysed by Fluorescence Correlation Spectroscopy to determine average numbers of molecules per vesicles. EVs were analysed before and after lysis with NP40s to determine molecular brightness (CPP: counts per particle) or number of freely diffusing fluorescent molecules (PN: particle number). The average number of molecules per EV was determined based on the relative increase in particle number (x-axis) or relative decrease in molecular brightness (y-axis), after additionally accounting for quenching as well as non-vesicular GFP (Corso et al., 2019). Crispr: GFP engineered into the human CD63 locus in HEK293T cells. OE: random integration of CD63-GFP in HEK293T cells. emGFP: Transient transfection of HEK293T cells with a CD63-emGFP expression plasmid. mNeon: high expressing clone from a HEK293T cell line stably expressing CD63-mNeon. (b) Correlation of mean single EV fluorescence intensities determined by single vesicle imaging and EVAnalyzer analysis with average number of FP molecules per particle determined by FCS of the same samples. Representative images are shown in the right panel. (c) Single vesicle intensity distribution for all samples. Histograms for 900 randomly selected spots each are shown. Binning: 5000 a.u.: arbitrary units (relative intensity from 16 bit grayscale image). Σ intensity per particle = area \times mean pixel intensity per spot.

vesicle remained relatively stable, irrespective of the plasmid concentration. This suggests that the population of vesicles carrying the transgenic CD63 might carry generally higher numbers of CD63 molecules than vesicles with endogenous CD63 only. This was confirmed by dissecting the intensity of anti-CD63 antibody labelling for the respective subpopulations, demonstrating that CD63 antibody signals were significantly higher for CD63-emGFP positive than CD63-emGFP negative vesicles within the same conditioned medium (Figure 5f). A more detailed analysis of the 2D single vesicle intensity distributions indeed confirmed a correlation of AlexaFluor555 anti-CD63 antibody labelling with the CD63-emGFP intensities (Figure 5g).

3.6 | Single vesicle imaging for optimisation of multiplexed genetic EV engineering

Using an optimal PEI/plasmid concentration derived from these data (4–8 μg plasmid per T25 flask), we next illustrate the application of EVAnalyzer to assess optimal conditions for EV engineering with multiple receptors. Fluorescent protein tagged tetraspanin constructs were combinatorially transfected into HEK293T cells (Supplementary Figure 1b) and EVs were again quantified directly in conditioned medium. As illustrated in Figure 6a (left panel), CD63-mCherry was co-transfected with emGFP tagged CD63, CD9 or CD81 either in combined (i) or separate (ii) lipoplexes. As negative control, the constructs were transfected individually in separate flasks and conditioned media were mixed for imaging (iii). In addition, we used a CD63-mCherry-emGFP fusion construct (iv). The colocalisation data in Figure 6a (right panel) demonstrate that a high fraction of double positive vesicles was observed for all single lipoplex combinations of the three tetraspanins (i), whereas this was substantially reduced when the constructs were transfected in separate lipoplexes (ii). This is plausible given that the probability of the same cells being transfected is lower when different constructs are applied in separate polymer vesicles. Interestingly, a small number of vesicles in the fusion construct sample showed signal only in either the GFP or the mCherry channels, which was assigned correctly by EVAnalyzer as assessed by visual inspection of the output control images. This can for example be explained by a small fraction of donor quenching due to FRET between the two fluorescent proteins (red only), or partial cleavage of the N-terminal mCherry (green only). Mixing conditioned media from either mCherry or emGFP transfected cells resulted in only

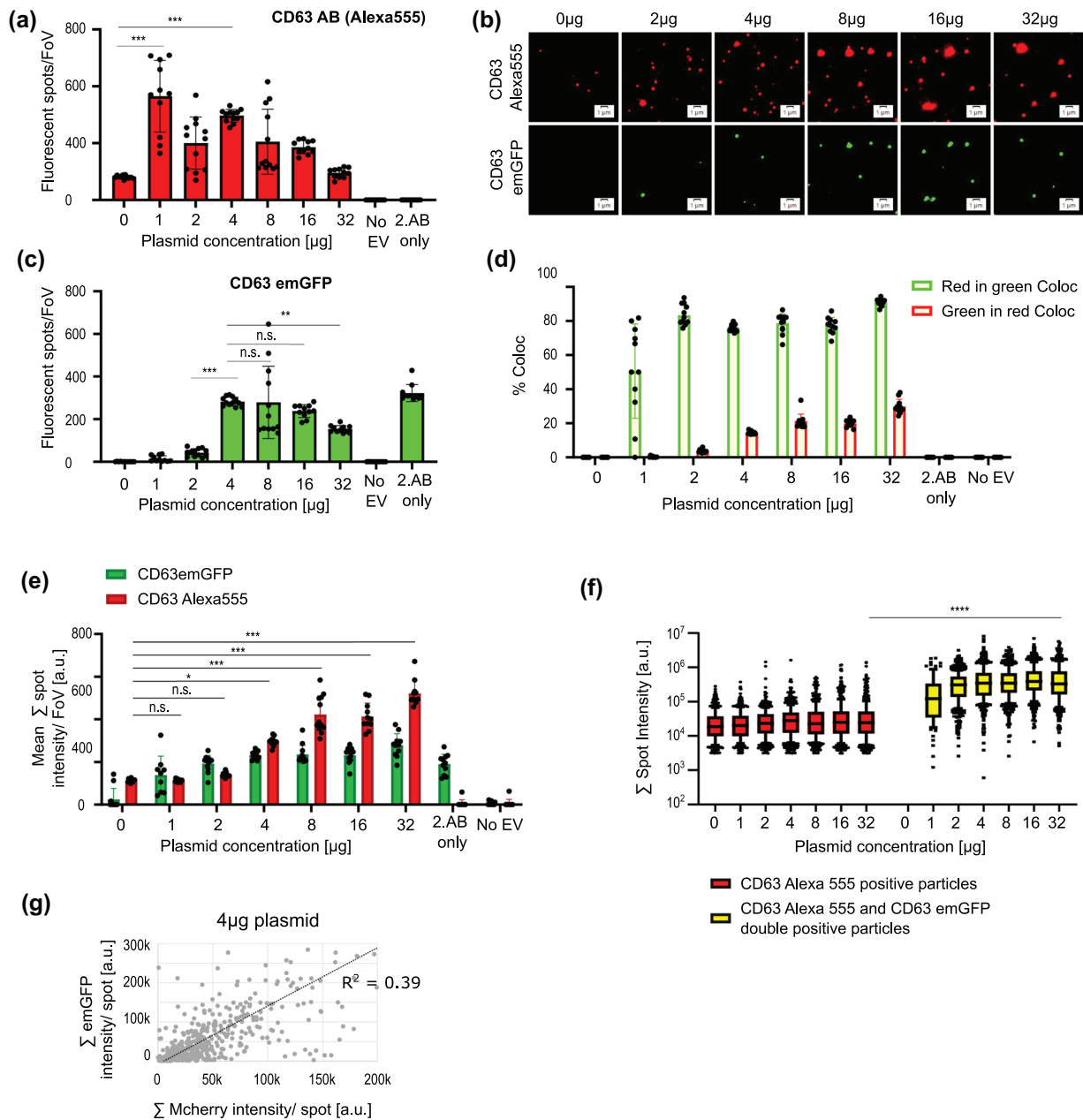


FIGURE 5 Optimisation of genetic EV engineering directly in conditioned media. (a-d) Optimisation of transfection conditions for CD63-emGFP transfection in HEK293T cells using immunolabelling and quantitative single vesicle imaging in conditioned medium following the optimised SOP (Supplementary File 4). The total number of anti-CD63 AlexaFluor555 positive spots (a) and the number of CD63-emGFP positive spots (c) was monitored as function of different plasmid/PEI concentrations used for transfection. Representative images are shown in (b) and % colocalization in (d). Samples with EVs but without primary antibody, as well as no-EV controls were used to control for unspecific binding. Statistics: Kruskal Wallis test (CD63 emGFP) or Welch's ANOVA test (CD63 AB AlexaFluor555); n.s. Non significant, ** $p < 0.01$, **** $p < 0.0001$. (e) Mean sum spot intensities in GFP and AlexaFluor555 fluorescence for all detected particles. Statistics: Kruskal Wallis test; n.s. Non significant, * $p < 0.017$, *** $p < 0.001$. (f) Mean sum spot intensities of AlexaFluor555 anti-CD63 positive particles separated for CD63-emGFP negative and positive particles. Data represent means from single vesicle distributions with box plots (log10 scale) showing the 10–90% percentile of the intensity distribution. Statistics: Man Whitney test; **** $p < 0.0001$. (g) 2D scatter dot plot of sum intensities of double positive particles (900 randomly selected spots from the 4 μg transfection sample) shows a positive correlation of CD63-emGFP fluorescence and anti-CD63 staining intensity in the AlexaFluor555 channel. a.u.: arbitrary units (relative intensity from 16 bit grayscale image). \sum intensity per vesicle = area \times mean pixel intensity per spot. All results were generated using the EVColoc pipeline with defined thresholds constant within the image series for each graph. Unless stated otherwise, data represent averages and standard deviations of 10 individual images and are representative for one out of at least three independent experiments.

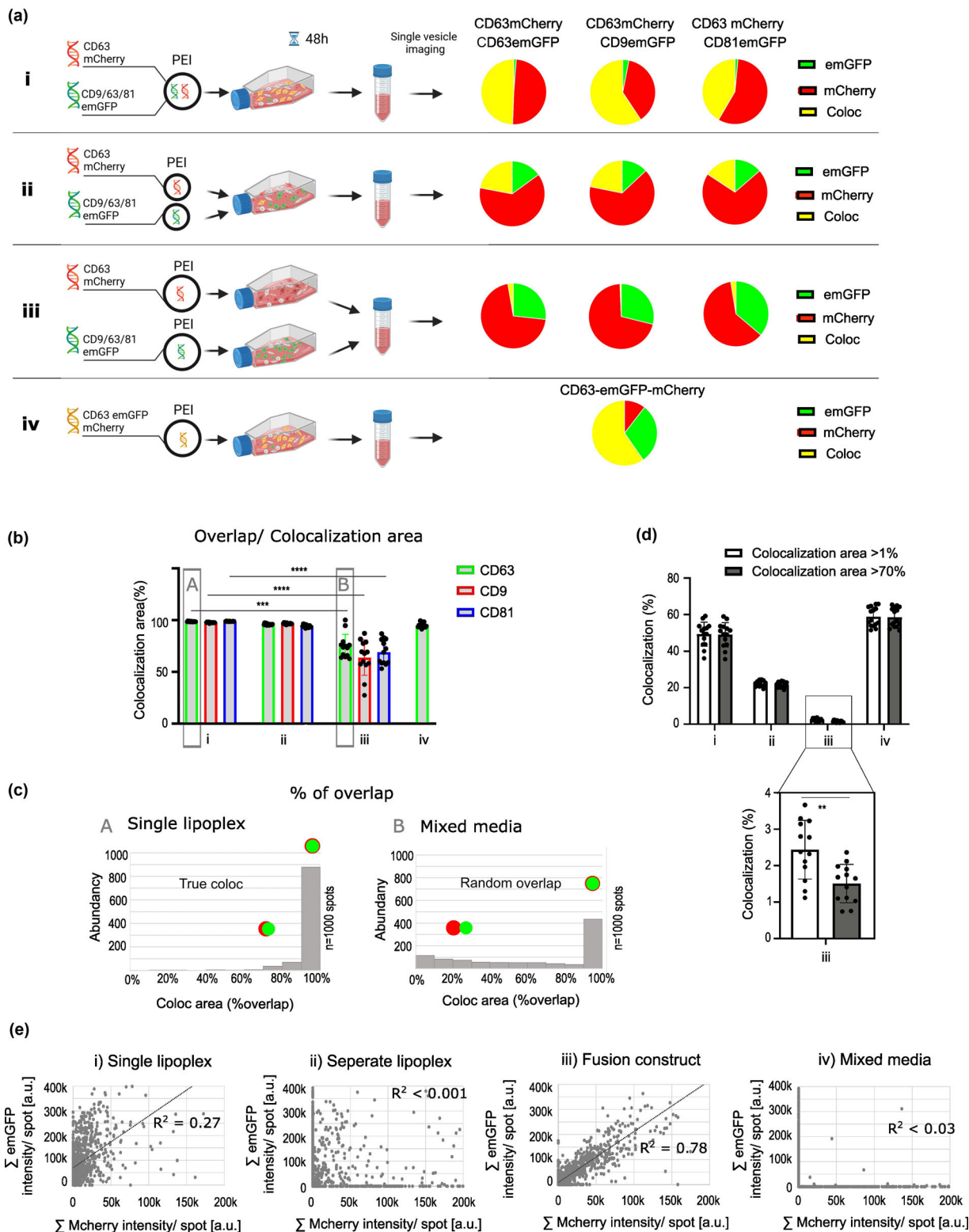


FIGURE 6 Optimisation of multiplexed genetic EV engineering. (a) HEK293T cells were co-transfected with CD63-mCherry and GFP tagged CD63, CD9 or CD81 either in combined lipoplexes (i) or separate lipoplexes (ii). Additionally, cells were transfected with the different constructs separately and conditioned media were mixed (iii). A CD63-emGFPmCherry fusion construct was used for comparison (iv). The percentage of GFP only, mCherry only, and double positive particles is shown in the pie charts. (b) The average overlap area of the double positive spots from each sample is shown in %. For the samples from the mixed media (iii), no double positive particles are expected and thus represent most likely random overlap. Statistics: Man Whitney U test for comparison of colocalisation area of CD63 single lipoplex (i) and CD63 mixed media (iii) and unpaired t test with Welch correction for the comparison of single lipoplex (i) and mixed media (iii) for CD9 and CD81; ***p < 0.001, ****p < 0.0001. (c) Single vesicle distribution histograms for overlap areas of double positive spots in a sample with true colocalisation (i) or random overlap (ii) as highlighted in panel (c). (d) % Colocalisation of CD63-mCherry with CD63-emGFP in the samples from the different transfection paradigms (i-iv) using % area overlaps as thresholds for colocalisation (white: > 1%; grey: > 70%). The inset shows the reduction of false positive colocalisation in the mixed medium control. Statistics: paired t-test to compare %colocalisation in colocalisation

(Continues)

FIGURE 6 (Continued)

are thresholded ($> 70\%$ colocalisation) versus non thresholded colocalisation analysis. $**p = 0.0013$. Green: mNeon fluorescence. Red: AlexaFluor555 fluorescence. Yellow: colocalisation. All results were generated using the EVColoc pipeline with defined thresholds constant within the image series for each graph. Data represent averages and standard deviations of 10 individual images and are representative for one out of at least three independent experiments. (e) 2D scatter dot plot analysis of CD63-emGFP and CD63-mCherry fluorescence from the different paradigms for double transfection. a.u.: arbitrary units (relative intensity from 16 bit grayscale image). Σ intensity per vesicle = area \times mean pixel intensity per spot. All results were generated using the EVColoc pipeline with defined thresholds constant within the image series for each graph. Unless stated otherwise, data represent averages and standard deviations of 10 individual images and are representative for one out of at least two independent experiments.

minimal counts of double positive vesicles (*iii*), validating the colocalisation analysis. As expected, the fraction of double positive vesicles was highest for the fusion construct (*iv*). While the number of false double positive vesicles in the negative control was negligible, an in-depth analysis of additional parameters provided by EVAnalyzer revealed that for these particles the mean overlap area between the two channels was smaller (Figure 6b (*iii*)). In contrast, the overlap area for the truly double positive vesicles in the control samples was between 90–100 % (Figure 6b (*iv*)). Such random overlap can be filtered out by setting a threshold for the minimal colocalisation area, which is facilitated by the single vesicle distribution of the colocalisation area (Figure 6c). Using a threshold of 70 % min overlap, re-analysis of the mixed CM controls reduced false positives by approximately two-fold, resulting in $< 2\%$ residual double positives (Figure 6d). These remaining false positives could represent either randomly occurring perfect overlay, aggregation or fusion. To facilitate such advanced colocalisation analysis we included an option for user defined colocalisation area threshold setting in the EVColoc pipeline (*'min coloc factor %'*). We would like to point out that these data additionally allow to assess the contribution of single spots representing more than one particle, which for the examples shown is less than 1.5% at optimized EVAnalyzer thresholds.

Further information on subpopulations can be obtained from 2D-scatter plots of the individual fluorescence intensities in the CD63-mCherry and CD63-emGFP detection channels (Figure 6e). Transfecting the two constructs in separate lipoplexes resulted in a lack of correlation between the emGFP and mCherry brightnesses (Figure 6e. (*ii*)), indicating random sorting of both fusion constructs into the same vesicle. In addition, the red only and green only vesicles were also apparent in the 2D brightness analysis, consistent with the low degree of colocalisation for this sample. Transfecting both constructs in one lipoplex showed a slightly increased tendency that vesicles with higher brightness of CD63-emGFP also comprise higher intensity of CD63-mCherry (Figure 6e (*i*)). This is consistent with the notion that the plasmids are introduced into the cells together thereby giving rise to more homogeneous distributions and expression ratios in the parent cells. As expected, EVs with the CD63-mCherry-emGFP fusion construct resulted in a high degree of correlation in the two-colour brightness distribution (Figure 6e (*iii*)) whereas the mixed media showed two independent, red and green only populations (Figure 6e. (*iv*)). Interestingly, double transfection of CD63-mCherry with either CD81-emGFP or CD9-emGFP resulted in only a poor correlation of single vesicle intensities even when transfecting the two constructs in the same lipoplex (Supplementary Figure 2a (CD81) and S2b (CD9)), indicating that loading densities of CD9 or CD81 do not correlate with loading densities of CD63 at the single vesicle level. These data exemplify how such single vesicle brightness distribution analysis can reveal subpopulations and provide further insight into whether two markers are sorted independently or are mechanically correlated.

3.7 | Application of EVAnalyzer for validation of EV labelling dyes at the single vesicle level

To track EV uptake and biodistribution in cells or in vivo, labelling with synthetic dyes is commonly used. In particular for EVs from sources incompatible with genetic manipulation, post-isolation biochemical labelling strategies are required. Many of these dyes bear additional advantages in chemical and biological stability and photophysical properties as compared to fluorescent proteins. However, since they typically rely on generic molecular interactions such as lipid anchoring or conjugation to amino acids, their specificity and stability are key issues. In many studies, the labelling of EVs is considered successful if the dye co-purifies with the vesicles. We propose that single vesicle analysis should be rigorously employed to judge which particles are labelled within a complex EV sample. To illustrate how EVAnalyzer enables such analysis, UF-SEC purified CD63-mNeon HEK293T EVs were labelled with Cy5 by NHS chemistry, MemGlow as well as DiI as three commonly used reagents (Figure 7). Both, Cy5-NHS as well as MemGlow resulted in nearly quantitative (ca 90 %) labelling of all CD63-mNeon positive EVs. The fraction of additionally labelled, non CD63-mNeon vesicles was higher for MemGlow than Cy5-NHS indicating an extra population of particles recognized by MemGlow in the samples. In contrast, the large majority of DiI labelled particles did not colocalise with CD63-mNeon, raising caution of interpreting results with this dye (Figure 7a).

EVs labelled with Cy5-NHS were generally brighter than particles labelled by MemGlow. Interestingly, the single vesicle intensity data revealed that the distribution of Cy5/CD63-mNeon double positive vesicles was shifted to substantially higher intensities as compared to Cy5 labelled, CD63-mNeon negative particles within the same sample—which was not observed for MemGlow (Figure 7b). CD63-mNeon is restricted to bona fide extracellular vesicles, whereas both dyes, Cy5 NHS as well as MemGlow may arguably label both, vesicles and non-vesicular particles in the sample. The different behaviour in the brightness shift of the

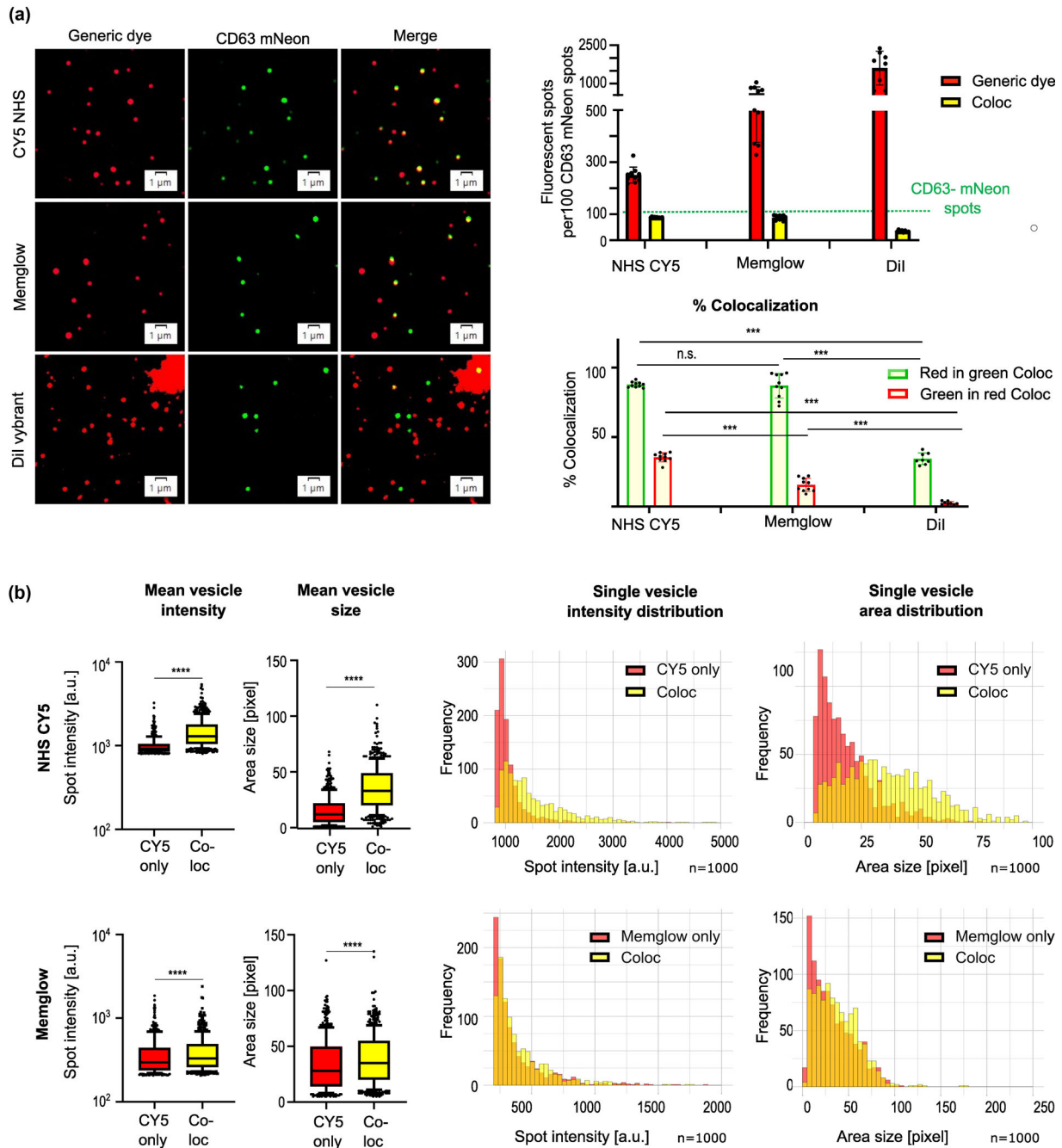


FIGURE 7 Post-isolation labelling of EVs with fluorescent dyes: validation by quantitative single vesicle imaging. (a) HEK293T CD63-mNeon EVs (UF-SEC purified) were labelled with either MemGlow, Cy5-NHS or DiI with removal of free dye as specified in the Materials & Methods section. Representative images (left panel) and quantification by EVAnalyzer (right panels) are shown. Green: mNeon fluorescence. Red: AlexaFluor555 fluorescence. Yellow: colocalization. Upper right panel: Total numbers of dye positive spots as well as total number of dye and CD63-mNeon double positive spots per FoV, normalised to 100 CD63-mNeon positive spots. Bottom right panel: % colocalization of CD63-mNeon positive spots labelled by the dye (red in green), and % of all dye labelled particles positive for CD63-mNeon (green in red). Statistics: Welch ANOVA test; n.s. Non significant, *** $p < 0.001$. (b) shows the spot intensity and spot area of the dye fluorescence of CY5 or MemGlow labelled particles. Single vesicle intensity and pixel area distributions of the dye fluorescence for 1000 randomly selected CD63-mNeon negative (red) or CD63-mNeon positive (yellow), dye labelled particles are shown. Left: box plots with 10%–90% percentile shown. Right: Frequency distribution histograms. a.u.: arbitrary units (relative intensity from 16 bit grayscale image). Statistics: Mann Whitney test; **** $p < 0.0001$. All results were generated using the EVColoc pipeline with defined thresholds constant within the image series for each graph. Data represent averages and standard deviations of 10 individual images and are representative for one out of at least three independent experiments.

two dyes may be explained by the fact that non-vesicular particles, such as lipoproteins, are less efficiently labelled by NHS ester chemistry due to their lower protein/particle content than EVs. Since the MemGlow-only particles have similar brightness as the CD63mNeon/MemGlow double positive particles, this would indicate that this dye in contrast labels CD63 positive and negative particles at similar stoichiometries.

3.8 | Single vesicle analysis of EVs from non-human sources by EVAnalyzer

EVs from non-human sources represent an increasingly relevant area in EV research and biomedical application development. The availability of tools such as antibodies for non-human EVs currently still poses a severe practical limitation, in particular with validation at the single vesicle level. To test how our described imaging protocols with single vesicle characterisation by EVAnalyzer may enable straightforward validation of cross-species use of EV detection tools, we characterised different antibodies for immunolabeling of bovine milk EVs (Figure 8). We first cloned mNeon-tagged expression constructs of bovine tetraspanins (CD63, CD81, CD9) for transfection into HEK293T cells (Supplementary File 3) in a side-by-side comparison with the corresponding human tetraspanin variants. The different genetically engineered EVs were immunostained with the corresponding CD63, CD9 or CD81 antibodies previously validated for human EVs (Figures 2, 3 and 5). Recognition of the human or bovine tetraspanins was assessed based on colocalisation with the corresponding FP-tagged receptors using EVAnalyzer (Figure 8a). Both, the CD9 as well as CD81 antibody cross-reacted with the bovine expression constructs with similar efficiency as for the human variants, with approximately 80–90 % of mNeon positive vesicles being recognised by the antibody (Figure 8b). In contrast, two different CD63 antibodies failed to effectively cross-react with bovine CD63, with only 5–15 % of mNeon positive vesicles being detected. Consistently, bovine CD9 and CD81 were both successfully detected by Western blotting of bovine milk derived EVs whereas no signal was obtained for CD63 (Figure 8c), despite confirmed presence of all tetraspanins by mass spectrometry-based proteomics (Figure 8d). Single vesicle imaging of bovine milk derived EVs labelled with Cy5 NHS resulted in positive signals for anti-CD9 (Figure 8e). Due to the difficulty of genetic engineering of milk EVs, it is not possible to directly control the specificity of antibody recognition in these samples, however, a majority of these particles colocalised with Cy5 signals (Figure 8e, right panel), which is in line with the specificity demonstrated on the EVs with bovine CD9-mNeon in Figure 8a. CD81 was not detected by imaging of milk EVs, however, also the signal intensity in Western blotting was very weak (Figure 8c) and the levels detected by MS-proteomics (Figure 8d) were substantially lower than CD9, suggesting that the abundance of CD81 in milk EVs might be too low to provide sufficient signal for single vesicle imaging. In line with the lack of cross-reactivity with bovine CD63-mNeon on HEK293T EVs, no signal was obtained for immunolabelling of milk derived EVs with the two CD63 antibodies (Figure 8e).

3.9 | EVAnalyzer can be applied to characterize synthetic nanoparticles

EVAnalyzer was primarily developed for EV research, however, is inherently applicable also for other types of nanoparticles as long they can be detected by fluorescence microscopy. A prototypical application area is the LNP (lipid-based nanoparticle) field, which has gained substantial momentum after the successful development and global application of LNP formulated mRNA vaccines for Covid19 (Baden et al., 2020). RNA encapsulation efficiencies by empty LNPs are typically determined indirectly such as by non-membrane permeable RNA intercalating dyes (Huang et al., 2022; Michel et al., 2017; Wu et al., 2008), or fractions of RNA co-isolating with liposomes, quantified by RT-qPCR (Saha et al., 2018; Tsuji et al., 2016). We reasoned that quantitative single particle imaging enabled by EVAnalyzer might provide a straightforward and direct method to characterise RNA encapsulation at the single particle level. To test this, fluorescently labelled LNPs were prepared with Cy5-DOPE (DODAG/DOPE/Cholesterol/CPA/Cy5-DOPE = 20:49.5:20:10:0.5 m/m/m/m/m) and used either empty or for encapsulation of AlexaFluor488-siRNA at a final mol charge ratio of 6:1 (ratio of positive charges of cationic lipids to negative charges of siRNAs, Figure 9a). NTA, light scattering and cryo-TEM analyses confirmed formation of spherical LNPs for both samples. LNPs with fluorescent siRNA showed a mean particle size of 154.6 ± 3.2 nm, a surface ζ -potential of 45.6 ± 2.0 mV and a polydispersity index (PdI) of 0.136 ± 0 , while for empty LNPs we measured a mean particle size of 124.5 ± 2.5 nm, a surface ζ -potential of 43.8 ± 2.2 mV and a PdI of $0.115 \pm 0.00+$ (Supplementary Figure 3a and S3b). The resulting siRNA-loaded LNPs were analysed by fluorescence imaging following protocols optimised for EVs, whereas positively charged microscope slides worked best for LNP immobilisation (data not shown). Cy5-labelled LNPs were well detectable by high-resolution widefield microscopy (Figure 9b), thereby allowing successful application of single vesicle quantification by EVAnalyzer (Figure 9c). Nearly 100 % of AlexaFluor488 signals were colocalised with Cy5-positive spots, directly demonstrating successful encapsulation of siRNA. Interestingly, the double positive particles comprised only ca 20 % of all LNPs visualised (Figure 9d), revealing that siRNA is not homogeneously encapsulated by all LNPs but rather accumulates in a subset of particles, at least at the tested stoichiometric ratio. A 2D scatter plot of Cy5 and AlexaFluor488 single particle sum intensities further demonstrates a weak positive correlation between the Cy5-lipid and siRNA signals (Figure 9e, $R^2 = 0.24$). Since the Cy5-DOPE density correlates directly with the LNP size, this indicates that

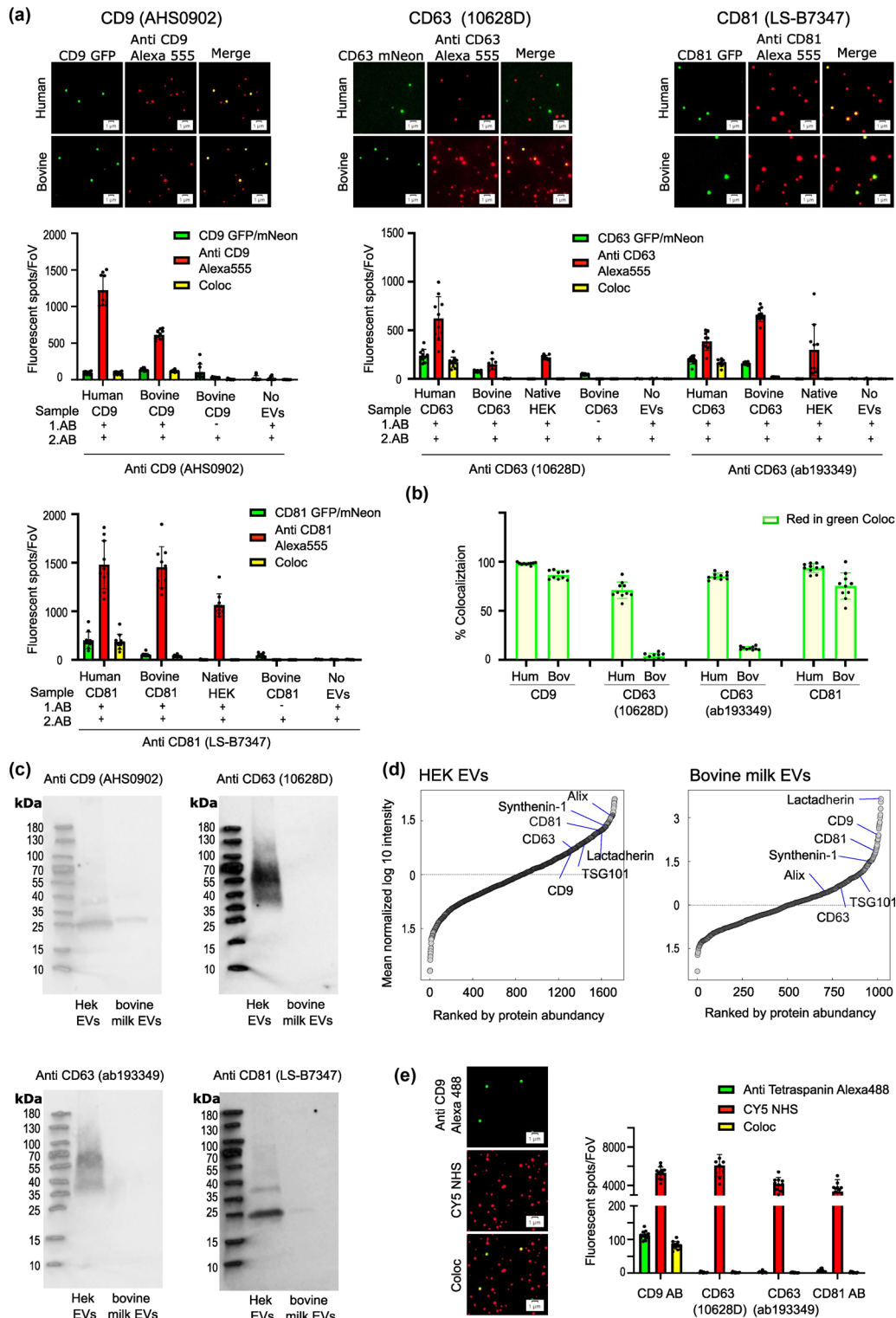


FIGURE 8 Species selectivity of tetraspanin antibodies quantified by single vesicle imaging. (a) EVs from HEK293T cells transiently transfected with expression constructs encoding either human or bovine tetraspanins fused to emGFP or mNeon were subjected to immunostaining with the corresponding anti-CD63, CD9 or CD81 antibodies as indicated. Representative images are shown in the top panels. Quantification of the total number of antibody positive (red), fluorescent protein positive (green) and double positive particles (yellow) are shown in the panels below. Controls without primary antibody as well as without EVs were used to determine antibody background signals. (b) % of Colocalization of FP-tagged tetraspanins detected by the corresponding antibodies (red in green). (c) Western blots of EVs from HEK293T cells or bovine milk with detection by the different tetraspanin antibodies as indicated. (d) Characterisation of EVs from HEK293T cells or bovine milk by HPLC-MS proteomics. Mean log₁₀ intensities of identified proteins were median-corrected and ranked by abundance. Depicted values are averages from three technical replicates each. tetraspanins and selected proteins are highlighted. (e) Immunostaining of EVs from bovine milk pre-labelled with Cy5-NHS. Representative images for CD9 detection are shown in the left panels, quantification of total fluorescent spots per FoV for all antibodies are shown in the right panel. CD63-mNeon negative (red) or CD63-mNeon positive (yellow), dye labelled particles as

(Continues)

FIGURE 8 (Continued)

indicated. All results were generated using the EVColoc pipeline with defined thresholds constant within the image series for each graph. Unless stated otherwise, data represent averages and standard deviations of 10 individual images and are representative for one out of at least three independent experiments.

siRNA is more likely loaded into larger LNPs. These data clearly demonstrate the application potential of single particle imaging enabled by EVAnalyzer for LNP characterisation and exemplify the level of information that can be obtained to guide formulation optimisation.

To test the scope of nanomaterials beyond EVs one step further, we applied EVAnalyzer on imaging data with mesoporous silica-based nanoparticles (SiO₂ NPs) loaded with fluorescent proteins (Figure 9f). β -lactoglobulin and lysozyme were labelled with TMR-NHS or Cy7-NHS, respectively, and purified by size exclusion chromatography on spin columns to remove excess free dye. Protein labelling efficiency and quantity were determined by RP-HPLC and SDS-PAGE (Supplementary File 5). Labelled proteins were loaded onto approximately 75 nm-sized mesoporous (approx. 4 nm pore size) SiO₂ NPs by physical adsorption either separately or in combination and protein loading was quantified as above (Supplementary File 5, Figures 1 and 2). The protein-coated particles were immobilised on QG slides following a similar protocol as optimised for EVs. Interestingly, in contrast to EVs the immobilisation of the SiO₂ NPs on regular QG slides or positively charged QG slides was not successful (data not shown). However, after pre-treatment of the glass surface with concentrated sulfuric acid/hydrogen peroxide (Piranha solution) to expose the -OH groups we were able to capture SiO₂ NPs for detection by fluorescence microscopy (Figure 9g). The particles showed an increased tendency for aggregation and cluster formation on the surface, which was not observed in suspension (Supplementary File 5, Table S1). In addition to the light diffraction limited spots, diffuse fluorescent background was observed, indicating a certain degree of protein dissociation from the particles, complicating the definition of the focal plane. Further, the fluorescence intensity was prone to rapid photobleaching during focus adjustment. This issue was resolved by spike-in of TetraSpeck (TS) beads into the sample, allowing to use the 488 nm spectral channel for focus adjustment. The obtained images, therefore, provided a stress test for single particle detection by EVAnalyzer. We used the pipeline 'EVColoc' and selected the 488 nm channel for TS bead removal. Additionally, we defined a size threshold of max. 500 pixel (corresponding to ca 2 μm^2 for the used optical settings) to filter out aggregates, and an intensity threshold adapted to the increased background fluorescence. As shown in Figure 9g (right panel), this allowed to selectively detect the light diffraction limited spots on the diffuse background signal, while efficiently removing the TS beads as well as the large clusters. Using these settings to analyse all samples allowed to quantify both, TMR- β -lactoglobulin—as well as Cy7-lysozyme-coated SiO₂ NPs (Figure 9h). Interestingly, the β -lactoglobulin-conjugated particles showed high variability between individual fields of view, whereas the lysozyme-conjugated particles were relatively homogeneously distributed. Further, the number per FoV was generally higher for β -lactoglobulin- than for lysozyme-conjugated SiO₂ NPs despite applying identical particle concentrations to the cover slides. This might indicate a lower conjugation efficiency of lysozyme, in line with a just very small difference in zeta potential value (Supplementary File 5, Table S1), and/or a reduced binding of these particles to the cover slide. Consistently, the combined loading resulted in a higher number of β -lactoglobulin than lysozyme-positive particles, with approximately 80 % of double-positive particles (Figure 9i, left panel). The mean sum intensity per particle was not reduced but slightly increased for combined loading of both proteins (Figure 9i, right panel), indicating that the loading of the two proteins is not competitive. Consistently, the single vesicle intensity distribution of the double coated particles showed a weak positive correlation between the two channels (Figure 9j, $R^2 = 0.39$), indicating that the loading of the two proteins was cooperative rather than competitive. Further in line with this conclusion, separating the population of particles from the combined loading into double and single positives (Figure 9k) reveals that the particles carrying both, lysozyme and β -lactoglobulin are shifted to higher intensities in both channels.

A more routine application of single vesicle imaging for non-biological, respectively, inorganic nanoparticles may clearly benefit from further optimisation of the experimental conditions. Nonetheless, we conclude that EVAnalyzer can already be successfully applied to single particle quantification of nanoparticles beyond extracellular vesicles, even on suboptimal microscopy images.

3.10 | Single-cell / single-vesicle quantification of EV cell uptake by EVAnalyzer pipelines

A recurring question in EV as well as nanoparticle research is the quantification of particle uptake into recipient cells. We therefore extended the EVAnalyzer features to enable quantification of internalised vesicles not only based on intracellular fluorescence intensities but also down to the single-vesicle / single-cell level. This requires both the identification of individual vesicles as well as image segmentation to define the cell area and segregation into single cells. We aimed to avoid the need for specific dyes to label the plasma membrane or cytosol. Instead, the EVAnalyzer pipeline was developed for cell area detection on brightfield images ('EVCount per total cell area'), whereas the segregation into individual cells requires nuclear stains only ('EVCount per cell'). Figure 10a shows the general workflow for processing images from cell uptake assays. For EV detection, the image is duplicated, blurred by applying a median filter, and subtracted from the original image. After additional smoothing, the same

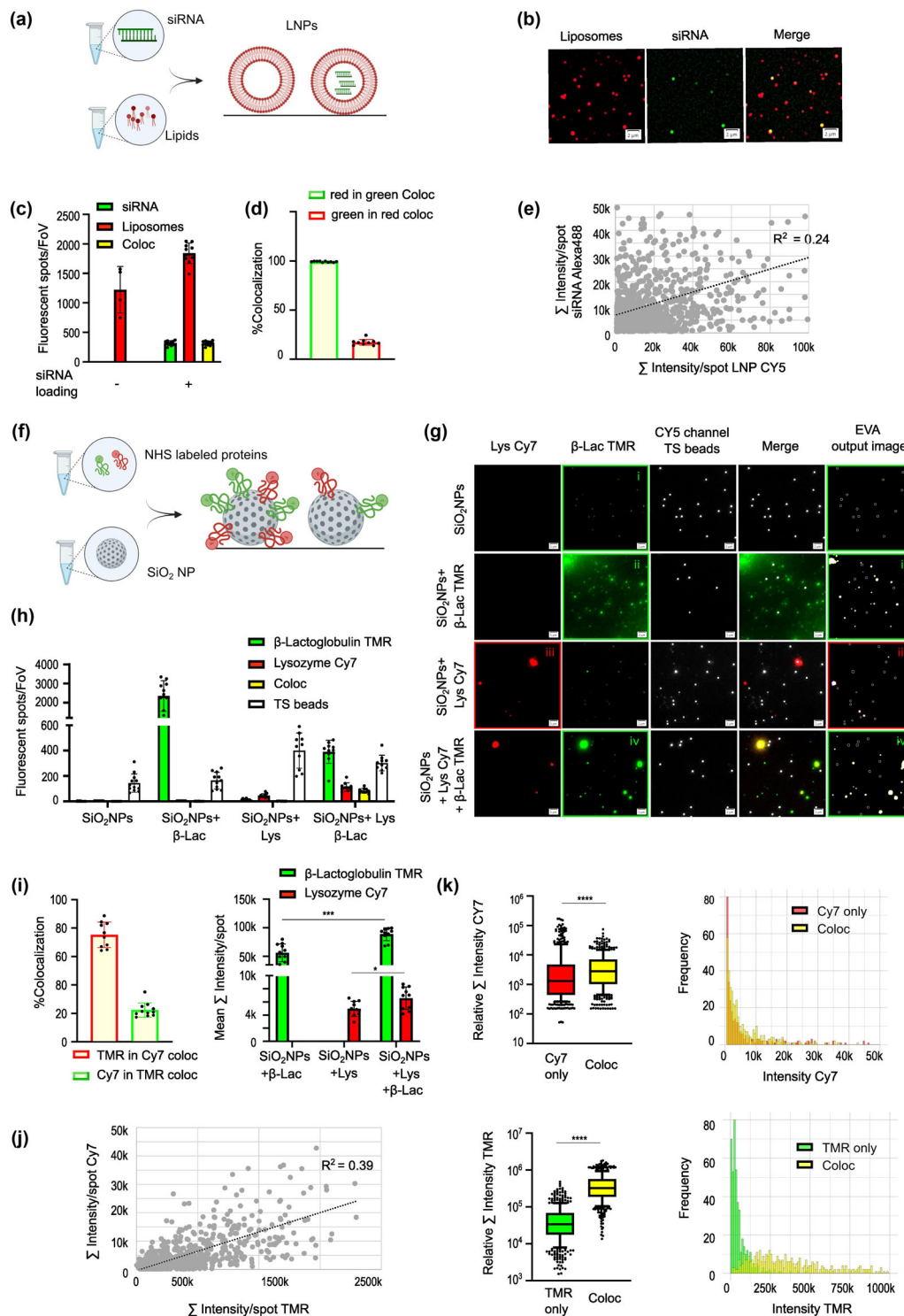


FIGURE 9 Application of EVAnalyzer for fluorescence imaging of synthetic nanoparticles. (a) Formulation of fluorescently labeled siRNA-loaded LNPs with Cy5-conjugated lipids and AlexaFluor488-labeled siRNA. (b) Representative images, (c) Total number of green and red fluorescent spots per FoV and (d) % Colocalization of fluorescently labeled siRNA-loaded LNPs (red: Cy5-lipids, green: AlexaFluor488-siRNA, yellow: colocalization). (e) 2D-scatter dot plot of single particle sum intensities of fluorescently labeled siRNA-loaded LNPs observing 1000 randomly selected spots in Cy5 and AlexaFluor488 channels. (f) Preparation of SiO₂ nanoparticles loaded with TMR-NHS labeled beta-lactoglobulin and/or Cy7-NHS labeled lysozyme. (g) Representative images and (h-k) EVA quantification of SiO₂ nanoparticles without any loading, with TMR-beta-lactoglobulin and/or Cy7-lysozyme. 100 nm TetraSpeck (TS) beads were spiked in and are fluorescent in all channels. The UV channel (405 nm excitation/410-455 nm emission; white) was used to filter out TS beads. The annotated output images as obtained by EVAnalyzer are shown in (g, right panels). The corresponding pairs of original and output images are highlighted by green or red frames and numbers. Detected spots are marked as white dots, objects which were filtered during TetraSpeck bead removal are indicated as white circles. (h) Total number of TMR (green), Cy7 (red) and double positive spots (yellow) per FoV for all samples as indicated. TS beads are shown in white. (i) % Colocalization for the particles from the double loading experiment (left panel) and mean sum intensities per particle for all samples (right panel). Statistics:

(Continues)

FIGURE 9 (Continued)

unpaired *t* test for Lysozyme Cy7 and Mann Whitney test for β -Lactoglobulin; **p* < 0.05, ****p* < 0.001. (j) 2D scatter dot plot of single particle intensities for 1000 randomly selected particles from the double loading experiment. (k) Single particle intensity distribution for either TMR, Cy7 or TMR/Cy7 double positive particles for 1000 randomly selected particles from the lysozyme/ β -lactoglobulin double loading experiment. Left: box plots (log10 scale), with 10–90% percentile shown. Right: Frequency distribution histograms. a.u.: arbitrary units (relative intensity from 16 bit grayscale image). Statistics: Mann Whitney test; *****p* > 0.0001. Σ intensity per particle = area \times mean pixel intensity per spot. All results were generated using the EVColoc pipeline with defined thresholds constant within the image series for each graph. Unless stated otherwise, data represent averages and standard deviations of 10 individual images and are representative for one out of at least three independent experiments.

steps as described for ‘CountEVs’ (Figure 1) are used for EV object recognition. In a second set of processing steps, the cellular area is assigned from a user-defined channel, whereas both, brightfield or fluorescence detection is suitable (‘Find Cell area’). The corresponding image is subjected to edge detection, smoothing and thresholding steps to create a cellular region of interest. Again, preview images are provided to facilitate manual threshold setting, however, auto thresholds have proven to work well for brightfield images. As a result, a binary image is created with only one region of interest, including all pixels assigned to the entire area of cells within a field of view. All detected EVs within this ROI can then be calculated (‘EVCount per total cell area’). Optionally, the total cell area can be further segregated into single cells (‘EVCount per cell’). This requires nuclear detection by, for example, DNA intercalating dyes such as DAPI or Hoechst, which is fed into the calculation of a Voronoi grid. This grid is then used to dissect the total cell area into individual cells. Optionally, cells which are only partially captured in the field of view can be eliminated based on lack or incomplete coverage of the nucleus (‘EV count per Cell- remove cropped cells’). To exemplify the process, we used Cy5-NHS labelled HEK293T CD63-mNeon EVs (Figure 7a) for uptake into A549 human lung epithelial cells at different concentrations. Cells were fixed after 60 min and nuclei were visualised with Hoechst. A typical image from widefield fluorescence microscopy (40x NA0.95) with maximum intensity projection of a z-stack is shown in Figure 10b, illustrating both the original image and processing results obtained by EVAnalyzer. It is worth mentioning that EVAnalyzer also provides an option for automated z-projection on serial images (max, min and average intensity projections), further minimising the need for manual image processing steps. Different options for quantification of the dose response data are shown in Figure 10c-i. A dose-dependent increase of EV internalisation can in principle already be inferred from total EV fluorescence intensity per total cell area (Figure 10c). However, in our example the Cy5-NHS ester labelling resulted in substantially higher brightness and number of labelled vesicles than CD63-mNeon fluorescence in the same sample (as demonstrated in Figure 7a). Accordingly, the increase in total mNeon signal within the cells was not sufficient to quantify the uptake based on total intensity on the background of the relatively high cellular autofluorescence in the 488 nm channel. Figure 10d demonstrates how this issue was resolved by detecting and quantifying the number of vesicles per cell, revealing a dose dependent saturation curve in both channels. Nearly all CD63-mNeon positive intracellular spots showed also Cy5 signal (> 90 %), consistent with the data obtained from single vesicle imaging of the same sample on coverslips (Figure 7a vs. Figure 10e). In contrast the fraction of Cy5 positive spots which also had CD63-mNeon fluorescence was reduced ca 2-fold after uptake and detection in the cells. This could be either due to a biased internalisation, or due to lower efficiency of mNeon fluorescence detection caused by cellular autofluorescence and/or quenching of mNeon within the cells. Additional features that can be extracted by EVAnalyzer are cellular size distribution histograms with an optional pixel-to- μ m correction (Figure 10f), histograms of EV numbers per cell (Figure 10g), as well as 2D correlations of all features (Figure 10h-i). For our uptake data, this reveals for example that the number of Cy5 and mNeon positive EVs detected within the cells increases linearly with the cell size (Figure 10f). Interestingly, a strong positive correlation was detected between the number of Cy5 and CD63mNeon EVs within the same cell. Given the low percentage of double positives, this indicates that both subpopulations (Cy5/CD63-mNeon double positives and Cy5-NHS positives/CD63-mNeon negatives) are taken up by the same cell with the same efficiency (Figure 10i).

4 | DISCUSSION

The complex biology of extracellular vesicles demands quantitative methods capable of resolving heterogeneous subpopulations at the single vesicle level (Arab et al., 2021). Methods like NTA and TRPS allow to determine the size and number of single particles and are now routinely used for basic characterisation of EV samples (Hartjes et al., 2019). However, individual populations of vesicles not only differ in size, density, or morphology, but also in their molecular composition. Consequently, there is a need to link molecular information to individual vesicles. TEM has been a gold standard for EV visualisation and in principle allows for detection of molecular markers on individual vesicles by immunogold labelling (Su et al., 2022). Since electron microscopy is generally limited in throughput and multiplexing possibilities, hard to standardise, and not readily accessible for every-day sample characterisation, orthogonal technologies are required. Extensions of the NTA technology to include multiple fluorescence channels is an emerging opportunity to combine size information from single particle tracking with fluorescent detection of EV markers. However, NTA is inherently biased against small particles and currently still limited in detection sensitivity (Desgeorges et al., 2020).

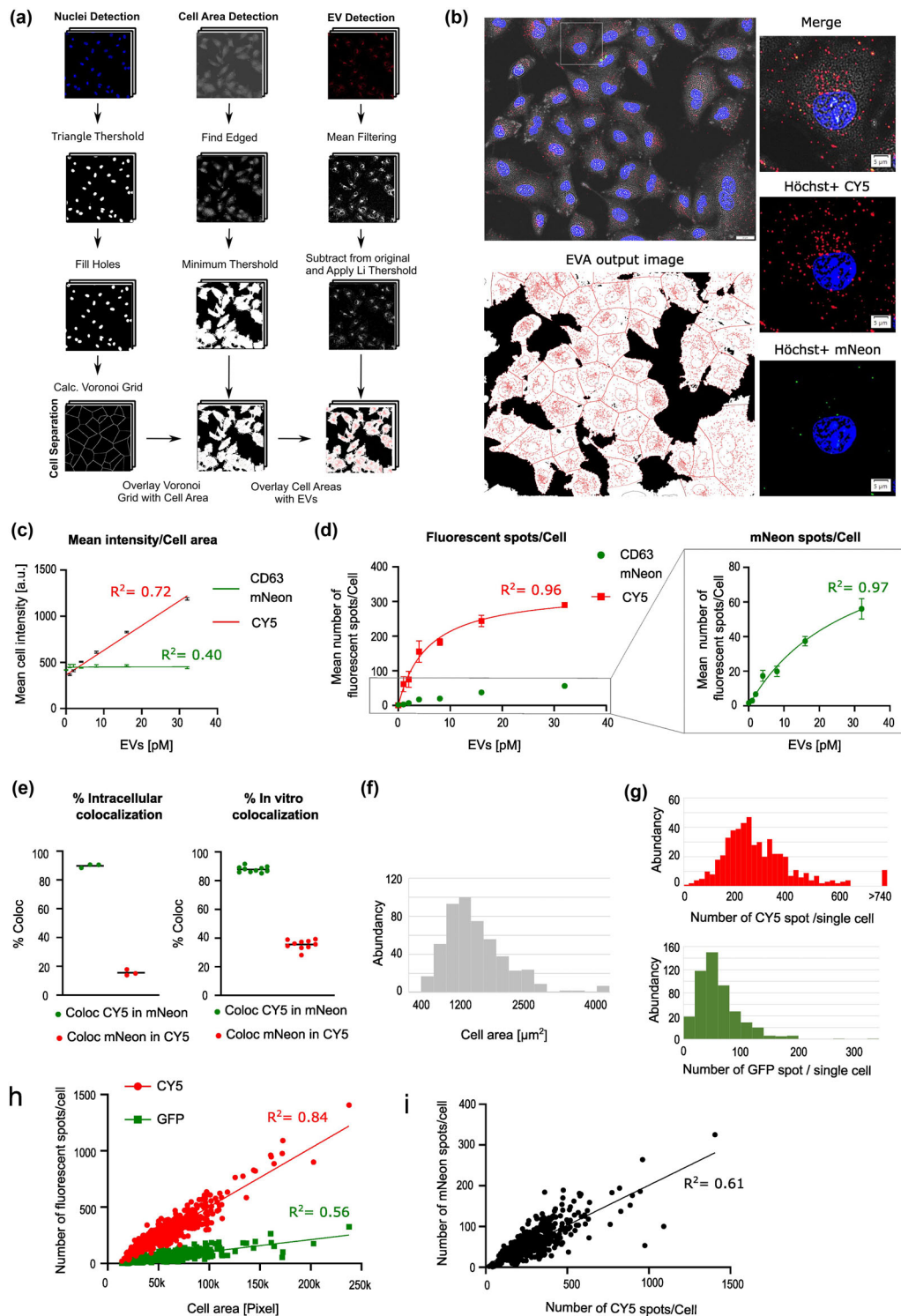


FIGURE 10 Quantitative high content imaging of EV uptake at the single cell–single vesicle level by EVAnalyzer. (a) Image processing workflow of the single cell–single vesicle quantification pipelines in EVAnalyzer. (b–i) Uptake of CD63-mNeon HEK293T EVs labelled with Cy5-NHS (Figure 7) in A459 human lung carcinoma cells. The cells were seeded in 96-well plates, incubated with different concentrations of EVs for 60 min, and imaged after washing, fixation and Hoechst33342 counterstaining. (b) Representative images are shown for the highest EV concentration (32 pM) as overlays from successively recorded channels. Blue: nuclei (Hoechst). Red: Cy5. green: CD63-mNeon. Greyscale: brightfield image. Top left: example overview image. Right panels: zoom in corresponding to the rectangle in the overview image with merge of all channels (top), Cy5/Hoechst (centre) and CD63-mNeon/Hoechst (bottom). Bottom left panel: corresponding output image generated by EVAnalyzer illustrating cell segmentation and EV object recognition. (c) Dose response of EV uptake quantified by mean intensity per total cell area or (d) numbers of fluorescent spots per cell. Right panel: zoom in for the CD63-mNeon spots/cell. Data represent averages from 16 FoV per well and three replicate wells each. Linear curve fit (c) or nonlinear fit (hyperbolic) for (d). (e) % Colocalization of intracellular EVs (mean from 16 individual FoV per well, each dot represents the mean value for one well of the 32 pM EV concentration) as compared to the % colocalization of the Cy5/Cd63mNeon HEK293T EVs prior to uptake (Cy5-NHS labelling in Figure 7, each dot represents an individual value from 10 different FoV). (f) Single

(Continues)

FIGURE 10 (Continued)

cell distribution of cell area and (g) Single cell distribution of the number of CD63-mNeon or Cy5 positive spots per cell. (h) Single cell correlation between cell area and the number of internalised CD63-mNeon (green) or Cy5 positive particles (red). (i) Single cell correlation of the number of CD63-mNeon versus Cy5 positive particles. Graphs in (f-i) show histograms or 2D-scatterplots of 1000 randomly selected cells from one well of the 32 pM EV concentration.

More recent developments which have impacted the field are based on advanced flow cytometry as well as surface capture methods. Key hurdles for EV flow cytometry are the low sensitivity of standard flow cytometers for particles smaller than approximately 200 nm in size, linked to pitfalls like coincidence, swarm detection and discrimination of antibody- or lipoprotein-mediated background artefacts (Görgens et al., 2019). A recent breakthrough was achieved by combining flow cytometry with imaging optics and CCD camera detection. In a systematic study, Gorgens and coworkers demonstrated the application of imaging flow cytometry (IMFC, commercialised by Luminex/Amnis Image Stream) for robust detection and quantification of EVs down to about 40 nm (Görgens et al., 2019), and meanwhile IMFC has seen more widespread use in the EV field (Li et al., 2022; Ricklefs et al., 2019; Tertel et al., 2022). Other approaches available are based on affinity-capture of EVs on surfaces followed by light microscopy using scattering and/or fluorescence detection by proprietary technologies, such as from NanoView ('ExoView') or Oxford Nanoimaging amongst the most advanced implementations (Nanoview; Nanoimager). These technologies have started to prove powerful for quantitative single vesicle characterisation in various EV research areas (e.g., Gomes et al., 2022; Melling et al., 2022; Silva et al., 2021; Wolf et al., 2022). The experimental challenges underlying robust single vesicle quantification of EVs and other submicron particles have created a need for guidelines in standardising and reporting. The recently published MIFlowCyt-EV framework has addressed this for flow cytometry studies of EVs (Welsh et al., 2020).

Commercialised platforms like IMFC, NanoView or ONI generally require integrated systems of specialised equipment, materials, and proprietary software. The significant costs and required expert operator know-how limit the application primarily to labs highly specialised in EV research. This complicates a broad implementation across the dramatically growing community of researchers interested in EV biology. Since these technologies are proprietary in nature, they are inherently not open to community development. Also, they still face technical limitations such as a sensitivity-based size limit of currently ca 40–200 nm in flow cytometry or detection biases due to affinity capture.

We and others have shown that EVs are well suited for detection and single particle tracking by both confocal (Corso et al., 2019; Heusermann et al., 2016; Tian et al., 2010) as well as wide field fluorescence microscopy (Bağcı et al., 2022; Burbidge et al., 2020; Corso et al., 2019). Single vesicles can be detected and quantified as light diffraction limited spots after intrinsic labelling with FP-tagged marker proteins (Corso et al., 2019; Heusermann et al., 2016) or immunostaining (Bağcı et al., 2022; Burbidge et al., 2020; Han et al., 2021; Hartjes et al., 2020) when immobilised on optical surfaces. More recent studies have focused on more advanced microscopy techniques for imaging of individual EVs using custom developed TIRF (Han et al., 2021) or single molecule localisation microscopy setups (Strohmeier et al., 2021). Despite the development of these highly specialised applications, the fact that even standard widefield fluorescence microscopes can be used (Corso et al., 2019) provided an ideal starting point to derive a more generically usable, straightforward process for single vesicle quantification with standard laboratory equipment. This required both, robust, generically applicable SOPs and possibilities for automated image analysis. Notably, several commercial image analysis softwares provide features for spot detection such as Imaris/Bitplane, MatLab, as well as ScanR or other professional high content screening software. The fact that none of these, often costly proprietary tools have so far been widely applied in the EV field is symptomatic of the need for open access, simple tools tailored to EV applications.

Fiji in contrast has grown into a widely used platform for microscope image analysis due to the open access–open-source code spirit, enabling community development efforts. To date, several algorithms have been developed for spot detection in microscopy images (Smal et al., 2010). Different Fiji plugins are available for spot detection in images ranging from microscopy of biological samples to astronomy, (e.g., ComDet or BIII (Katrukha, 2020; Kozubek & B, 2013)). So far, these are limited to manual, image-by-image analysis, not allowing for automated batch processing, and have also not been systematically tested, optimised, and validated for EV applications. The development of EVAnalyzer was therefore originally driven by our own need for a robust, straightforward, and user-friendly open access tool for automated image analysis to enable routine, high content single vesicle quantification. Developed by and for EV researchers in collaboration with programmers, EVAnalyzer was optimised and systematically tested for key applications in the EV research field. In our experience, the batch processing capability for automated analysis of large sets of images within one experimental series is an essential feature for practical use. First, it provides the throughput needed for routine analysis of larger sets of EV samples, where additionally technical replicate samples and multiple images per sample are advisable to obtain statistically significant quantitative data. Secondly, it ensures identical processing of all images within one series and comparability of results within the same experiment. The parameter setting for batch processing is facilitated by preview images in the GUI which illustrate the vesicle detection on the original images.

Notably, it is difficult to obtain a ground truth for real EV samples since the absolute number of EVs adhering to the glass slide is unknown. Also, the spot detection with any kind of analysis will always depend on relative threshold setting and classification criteria—whether defined by human or artificial intelligence. Therefore, it is currently not possible to assess how many spots in a realistic image truly correspond to EVs. Synthetic images as a possible alternative would, however, again comprise a bias of

what signal to noise is to be expected for different EV preparations. For validation of image analysis by EVAnalyzer, we therefore used experimentally obtained images of EV samples with subjective object classification by the human eye as a benchmark. A comparative study confirmed that automated analysis by EVAnalyzer obtained outputs very similar to the average results obtained by blinded, image-by-image analysis by four independent EV researchers. A certain operator bias was observed for manual image analysis, which was minimised when the same four persons used EVAnalyzer, whereas the analysis time for the same set of images was reduced from ca 40 min to < 2 min. Despite this validation of automated image processing by EVAnalyzer on representative, real EV samples, we advise to routinely spot check the results from automated batch processing for each analysis session. This is facilitated by the annotated output images, which are provided for each of the original images in the EVAnalyzer output files and allow scrutinising the settings for the automated image processing. The numerical data are provided in a systematically structured Excel file, with an overview sheet summarising the results for each image, hyperlinked to individual worksheets per image listing the data of each individual vesicle and cell.

EVAnalyzer was optimised and tailored to answer typical questions in the EV research requiring single vesicle quantification, including the multiplexed characterisation of subpopulations based on immunostaining of EV markers, optimisation of genetic engineering, estimation of molecular loading densities, quantitative validation of antibodies for EV surface proteins in situ or determining the specificity and efficiency of EV labelling with fluorescent dyes. We particularly aimed to provide a SOP for EV immobilisation and immunostaining that is entirely based on standard materials and reagents, and compatible with imaging on standard fluorescence microscopes. This procedure was validated for both, purified and crude EV samples from diverse sources and species, ranging from human cell line-derived EVs to food-derived EVs. Notably, the EV capture and immunostaining protocol can even be applied directly in conditioned medium, which is a major benefit for practical use. In consequence, the procedure can be used, for example, for rapid assessment of EV sample quality during conditioning, using only 30–50 μ l aliquots directly from the cell supernatant, thereby limiting the amount of required material, saving time and effort needed for sample clean up and additionally avoiding any bias by EV purification protocols. Our SOP has so far been well established for detection of FP-tagged EVs, fluorescently labelled EVs or immunolabelling of surface markers. We would like to note that immunolabelling of luminal cargo has not been successful so far in our hands since the permeabilization resulted in loss of EVs from the surface, potentially due to lysis. Burbidge *et al.* reported immunolabelling of Tsg101 in EVs permeabilized by Saponin after immobilisation by spinoculation (Burbidge *et al.*, 2020), although lacking validation of the antibody labelling with, for example, FP-tagged Tsg101. It is therefore conceivable that detection of luminal proteins using our SOP may be possible with additional optimisation of the permeabilization conditions. While we primarily intended to develop a process for relative rather than absolute quantification of EV subpopulations, the number of EVs unspecifically captured on regular quartz glass surfaces correlated remarkably well with the concentration in solution, at least within two orders of magnitude. We anticipate that either by spiking in internal standards, such as orthogonally labelled EVs, or measuring corresponding standard curves it may even be possible to back calculate from the number of captured EVs to the absolute concentration in solution. While this will require systematic validation for each specific type of EV sample, the ‘TS removal option’ of EVAnalyzer already provides a feature allowing for detection, quantification and subtraction of reference vesicles or beads.

As a second major application area of EVAnalyzer, we developed specific pipelines for quantifying EV uptake at the single-cell/single-vesicle level. Uptake of EVs is often quantified by bulk fluorescence using flow cytometry which provides the required throughput for statistical analysis. Monitoring EV uptake by microscopy allows to reveal additional information such as the number of EVs per cell and their subcellular localisation, however, is primarily used for visualisation rather than quantification due to the need for automation; automated scanning microscopes as well as high throughput quantification tools are routinely used in industrial high throughput screening but often are not available in academic institutions. Addressing the latter, EVAnalyzer enables automated image batch processing required for quantitative imaging-based cell uptake assays, irrespective of the microscopy platform. Importantly, comparing EV numbers and bulk fluorescence per cell within the same experiment (Figure 10) revealed that counting EV numbers per cell can be more sensitive than bulk fluorescence, especially for dim EV labels and channels with high autofluorescence. In addition, a colocalisation analysis of individual spots may reveal information that is lost upon bulk fluorescence measurements. EVAnalyzer currently does not include any features for quantifying subcellular EV localisation, which may be subject to future community developments.

Current capabilities of EVAnalyzer comprise vesicle counts, colocalisation, and vesicle brightness as well as size, but notably the sizing of EVs based on spot analysis is not valid when diffraction limited microscopy is used. With the increasing availability of dSTORM, STED and other super-resolution technologies, sizing of EVs by fluorescence microscopy is, however, within reach. We therefore tested the analysis of dSTORM super-resolution images of EVs with single and multiple labels by EVAnalyzer (Supplementary File 8). To use the current version of the plugin, images need to be pre-processed to artificially bin clusters of blinking fluorophores into single spots. Thereby, EV numbers and colocalization can be quantified, but the size information is currently lost. Nevertheless, we anticipate that future adaptations should be straightforward to extract additional information from super-resolution images such as cluster size and sub-cluster numbers. With the source code accessible, EVAnalyzer may thus be a valuable community development platform to complement proprietary software for commercialised super-resolution technologies.

Given the robustness and simplicity of the process presented in this manuscript, we believe that further adaptations will enable also relative and absolute EV quantification in more complex samples such as serum, urine or histological sections, or advanced applications such as single vesicle imaging based enzymatic assays, some of which we are already testing. A more routine application of single vesicle imaging for non-biological, respectively, inorganic nanoparticles may clearly benefit from further optimisation of the experimental conditions. Nonetheless, based on the examples we highlight in this manuscript we conclude that EVAnalyzer can already now be successfully applied to single particle quantification of LNPs or other synthetic nanoparticles, even on suboptimal microscopy images. To date, we have already shared EVAnalyzer as well as our SOP with collaborating labs and beta-testers where the process has been successfully implemented and is already routinely used. Being now made generally available, we encourage further development of EVAnalyzer by the community, with feedback and post-publication tracking via GitHub (<https://github.com/joda01/evanalyzer/issues>). In conclusion, EVAnalyzer is a powerful, versatile, and easy-to-use tool for routine and widespread use both the EV and nanoparticle fields, as well as an ideal platform for open innovation for single vesicle imaging applications.

AUTHOR CONTRIBUTIONS

Melanie Schürz and Nicole Meisner-Kober devised the project and guided the experimental work; Joachim Danmayr programmed EVAnalyzer; Melanie Schürz and MJ developed the procedures for EV capture, (immuno)labelling and imaging and tested, validated and iteratively optimised EVAnalyzer in close collaboration with Joachim Danmayr, Jana Kiefer, Vesna Stanojlovic and Tanja Plank tested the process and contributed to optimisation for specific applications; Eva Klinglmayr, Heloisa Melo Benirschke, Melanie Schürz, Maria Jaritsch and Cristian-Tudor Matea isolated and characterised EV samples from different sources under guidance by Nicole Meisner-Kober and MHint; Constantin Blöchl performed the LC-MS proteomics characterisation under guidance by Christian G. Huber. Cryo-TEM was performed by Melanie Schürz and Nicole Meisner-Kober under guidance by Thomas Heuser. Patrick Zimmerebner and Eva Klinglmayr cloned the bovine FP-tetraspanin expression constructs for experiments performed by Jakob Rauter and Melanie Schürz, Martin Wolf, Fausto Gueths Gomes and Melanie Schürz performed the dSTORM experiments under guidance by DS and Nicole Meisner-Kober. Zdenek Kratochvil, Zbynek Heger and Andrew Miller designed and performed experiments with LNPs, LJ synthesised and characterised SiO₂ NPs under guidance by MHim and performed loading with fluorescently labelled proteins characterised by Cristian-Tudor Matea for imaging by Vesna Stanojlovic and Maria Jaritsch. All other experiments were performed by Melanie Schürz. Melanie Schürz and Nicole Meisner-Kober wrote the manuscript, which was read and edited by all co-authors.

ACKNOWLEDGEMENTS

We kindly thank Dr. Eva Rohde and Dr. Mario Gimona for helpful comments on our manuscript, Dr. Andre Görgens and Dr. Samir ElAndalousi (Karolinska Institute, Stockholm, Sweden) for providing stable CD63-mNeon expressing HEK293T cells, as well as Dr. Mario Maierhofer and Dr. Jaroslav Jacak (Fachhochschule Upper Austria/Linz, Austria) for providing HEK293T cells with CRISPR-Cas9 mediated genomic integration of GFP into the CD63 locus ('CD63 CRISPR') or random genomic integration of CD63-GFP ('CD63 OE'). We also acknowledge the Cryo-Electron Microscopy and Tomography Core Facility supported by the Czech Ministry of Education, Youth and Sports (MEYS CR, LM2018127). This work was supported by the following grants: EV-Quant (County of Salzburg, WISS2025, 20102-F2100572-FPR); EV-TT BPro (County of Salzburg, WISS2025, P1812596), EVTT (European Union, EFRE/IWB 20102-F1900731-KZP), FWF grant W01213, EC H2020 NanoCommons 731032 and AF-IGA2021-IP057. ZK would like to express his gratitude to Brno PhD Talent. ADM wishes to thank MEYS ČR for the award of OPVVV Project FIT (Pharmacology, Immunotherapy, NanoToxicology), (CZ.02.1.01/0.0/0.0/15_003/0000495) that is financially supported by the European Regional Development Fund.

CONFLICTS OF INTEREST

ADM is a shareholder in KP Therapeutics (Europe) s.r.o. The remaining authors would like to declare no conflicts of interest.

ORCID

Melanie Schürz  <https://orcid.org/0000-0003-0170-3261>

Martin Wolf  <https://orcid.org/0000-0002-4795-8086>

REFERENCES

- Arab, T., Mallick, E. R., Huang, Y., Dong, L., Liao, Z., Zhao, Z., Gololobova, O., Smith, B., Haughey, N. J., Pienta, K. J., Slusher, B. S., Tarwater, P. M., Tosar, J. P., Zivkovic, A. M., Vreeland, W. N., Paulaitis, M. E., & Witwer, K. W. (2021). Characterization of extracellular vesicles and synthetic nanoparticles with four orthogonal single-particle analysis platforms. *Journal of Extracellular Vesicles*, 10(6), e12079. [CrossRef].
- Baden, L. R., El Sahly, H. M., Essink, B., Kotloff, K., Frey, S., Novak, R., Diemert, D., Spector, S. A., Rouphael, N., Creech, C. B., Mcgettigan, J., Khetan, S., Segall, N., Solis, J., Brosz, A., Fierro, C., Schwartz, H., Neuzil, K., Corey, L., & Zaks, T. (2020). Efficacy and safety of the mRNA-1273 SARS-CoV-2 vaccine. *New England Journal of Medicine*, 384(5), 403–416. [CrossRef].

- Bağcı, C., Sever-Bahçekapılı, M., Belder, N., Bennett, A. P. S., Erdener, S. E., & Dalkara, T. (2022). Overview of extracellular vesicle characterization techniques and introduction to combined reflectance and fluorescence confocal microscopy to distinguish extracellular vesicle subpopulations. *Neurophotonics*, 9(2), 021903.[CrossRef].
- Bordanaba-Florit, G., Royo, F., Kruglik, S. G., & Falcón-Pérez, J. M. (2021). Using single-vesicle technologies to unravel the heterogeneity of extracellular vesicles. *Nature Protocols*, 16(7), 3163–3185.[CrossRef].
- Burbidge, K., Zwickelmaier, V., Cook, B., Long, M. M., Balva, B., Lonigro, M., Ispas, G., Rademacher, D. J., & Campbell, E. M. (2020). Cargo and cell-specific differences in extracellular vesicle populations identified by multiplexed immunofluorescent analysis. *Journal of Extracellular Vesicles*, 9(1), 1789326.[CrossRef].
- Claridge, B., Lozano, J., Poh, Q. H., & Greening, D. W. (2021). Development of extracellular vesicle therapeutics: Challenges, considerations, and opportunities. *Frontiers in Cell and Developmental Biology*, 9, 734720.[CrossRef].
- Colombo, M., Moita, C., van Niel, G., Kowal, J., Vigneron, J., Benaroch, P., Manel, N., Moita, L. F., Théry, C., & Raposo, G. (2013). Analysis of ESCRT functions in exosome biogenesis, composition and secretion highlights the heterogeneity of extracellular vesicles. *Journal of Cell Science*, 126(Pt 24), 5553–5565.
- Corso, G., Heusermann, W., Trojer, D., Görgens, A., Steib, E., Voshol, J., Graff, A., Genoud, C., Lee, Y., Hean, J., Nordin, J. Z., Wiklander, O. P. B., El Andaloussi, S., & Meisner-Kober, N. (2019). Systematic characterization of extracellular vesicle sorting domains and quantification at the single molecule - single vesicle level by fluorescence correlation spectroscopy and single particle imaging. *Journal of Extracellular Vesicles*, 8(1), 1663043.[CrossRef].
- Corso, G., Mäger, I., Lee, Y., Görgens, A., Bultema, J., Giebel, B., Wood, M. J. A., Nordin, J. Z., & El Andaloussi, S. (2017). Reproducible and scalable purification of extracellular vesicles using combined bind-elute and size exclusion chromatography. *Science Reports*, 7(1), 11561.
- Cox, J., & Mann, M. (2008). MaxQuant enables high peptide identification rates, individualized p.p.b.-range mass accuracies and proteome-wide protein quantification. *Nature Biotechnology*, 26(12), 1367–1372.[CrossRef].
- Dar, G. H., Mendes, C. C., Kuan, W. - L., Speciale, A. A., Conceição, M., Görgens, A., Uliyakina, I., Lobo, M. J., Lim, W. F., El Andaloussi, S., Mäger, I., Roberts, T. C., Barker, R. A., Goberdhan, D. C. I., Wilson, C., & Wood, M. J. A. (2021). GAPDH controls extracellular vesicle biogenesis and enhances the therapeutic potential of EV mediated siRNA delivery to the brain. *Nature Communication*, 12(1), 6666.[CrossRef].
- De Groot, M., Hintersteiner-Wenzel, M., Manzotti, R., & Meisner, N. C. (2021). Inventors. *EvoBiotiX SA. Extracellular vesicles from milk and process for isolating the same*. CH070433/2021, filing date October 22, 2021.
- Desgeorges, A., Hollerweger, J., Lassacher, T., Rohde, E., Helmbrecht, C., & Gimona, M. (2020). Differential fluorescence nanoparticle tracking analysis for enumeration of the extracellular vesicle content in mixed particulate solutions. *Methods (San Diego, Calif.)*, 177, 67–73.
- Dooley, K., Mcconnell, R. E., Xu, K., Lewis, N. D., Haupt, S., Youniss, M. R., Martin, S., Sia, C. L., McCoy, C., Moniz, R. J., Burenkova, O., Sanchez-Salazar, J., Jang, S. C., Choi, B., Harrison, R. A., Houde, D., Burzyn, D., Leng, C., Kirwin, K., & Williams, D. E. (2021). A versatile platform for generating engineered extracellular vesicles with defined therapeutic properties. *Molecular Therapy*, 29(5), 1729–1743.[CrossRef].
- Eckhard, U., Blöchl, C., Jenkins, B. G. L., Mansfield, M. J., Huber, C. G., Doxey, A. C., & Brandstetter, H. (2020). Identification and characterization of the proteolytic flagellin from the common freshwater bacterium *Hylemonella gracilis*. *Scientific Reports*, 10(1), 19052.[CrossRef].
- Essandoh, K., Yang, L., Wang, X., Huang, W., Qin, D., Hao, J., Wang, Y., Zingarelli, B., Peng, T., & Fan, G. -C. (2015). Blockade of exosome generation with GW4869 dampens the sepsis-induced inflammation and cardiac dysfunction. *Biochimica Et Biophysica Acta*, 1852(11), 2362–2371.[CrossRef].
- Gomes, F. G., Andrade, A., Wolf, M., Hochmann, S., Krisch, L., Maeding, N., Regl, C., Poupardin, R., Ebner-Peking, P., Huber, C. G., Meisner-Kober, N., Schallmoser, K., & Strunk, D. (2022). Synergy of human platelet-derived extracellular vesicles with secretome proteins promotes regenerative functions. *Biomedicine*, 10(2), 238.[CrossRef].
- Görgens, A., Bremer, M., Ferrer-Tur, R., Murke, F., Tertel, T., Horn, P. A., Thalmann, S., Welsh, J. A., Probst, C., Guerin, C., Boulanger, C. M., Jones, J. C., Hanenberg, H., Erdbrügger, U., Lannigan, J., Ricklefs, F. L., El-Andaloussi, S., & Giebel, B. (2019). Optimisation of imaging flow cytometry for the analysis of single extracellular vesicles by using fluorescence-tagged vesicles as biological reference material. *Journal of Extracellular Vesicles*, 8(1), 1587567.[CrossRef].
- Gupta, D., Wiklander, O. P. B., Görgens, A., Conceição, M., Corso, G., Liang, X., Seow, Y., Balusu, S., Feldin, U., Bostancioglu, B., Jawad, R., Mamand, D. R., Lee, Y. X. F., Hean, J., Mäger, I., Roberts, T. C., Gustafsson, M., Mohammad, D. K., Sork, H., & El-Andaloussi, S. (2021). Amelioration of systemic inflammation via the display of two different decoy protein receptors on extracellular vesicles. *Nature Biomedical Engineering*, 5(9), 1084–1098.[CrossRef].
- Han, C., Kang, H., Yi, J., Kang, M., Lee, H., Kwon, Y., Jung, J., Lee, J., & Park, J. (2021). Single-vesicle imaging and co-localization analysis for tetraspanin profiling of individual extracellular vesicles. *Journal of Extracellular Vesicles*, 10(3), e12047.[CrossRef].
- Hartjes, T., Mytnyk, S., Jenster, G., Van Steijn, V., & Van Royen, M. (2019). Extracellular vesicle quantification and characterization: Common methods and emerging approaches. *Bioengineering*, 6(1), 7.[CrossRef].
- Hartjes, T. A., Slotman, J. A., Vredenburg, M. S., Dits, N., van der Meel, R., Duijvesz, D., Kulkarni, J. A., French, P. J., Van Capellen, W. A., Schiffelers, R. M., Houtsmuller, A. B., Jenster, G. W., & Van Royen, M. E. (2020). EVQuant; high-throughput quantification and characterization of extracellular vesicle (sub)populations. *bioRxiv*, <https://doi.org/10.1101/2020.10.21.348375>
- Heusermann, W., Hean, J., Trojer, D., Steib, E., Von Bueren, S., Graff-Meyer, A., Genoud, C., Martin, K., Pizzato, N., Voshol, J., Morrissey, D. V., Andaloussi, S. E. L., Wood, M. J., & Meisner-Kober, N. C. (2016). Exosomes surf on filopodia to enter cells at endocytic hot spots, traffic within endosomes, and are targeted to the ER. *Journal of Cell Biology*, 213(2), 173–184.[CrossRef].
- Huang, Y., Zheng, S., Guo, Z., De Mollerat Du Jeu, X., Liang, X. - J., Yang, Z., Zhang, H. - Y., Gao, S., & Liang, Z. (2022). Ionizable liposomal siRNA therapeutics enables potent and persistent treatment of Hepatitis B. *Signal Transduction and Targeted Therapy*, 7(1), 38.[CrossRef].
- Juan, T., & Fürthauer, M. (2018). Biogenesis and function of ESCRT-dependent extracellular vesicles. *Seminars in Cell & Developmental Biology*, 74, 66–77.[CrossRef].
- Katrakha, E. (2020). Imagej plugin detecting and colocalizing particles of given size (vesicles, dots, etc on Biological Microscopy Images); Available from: <https://github.com/ekatrakha/ComDet>
- Kolli, S., Wong, S. - P., Harbottle, R., Johnston, B., Thanou, M., & Miller, A. D. (2015). pH-triggered nanoparticle mediated delivery of siRNA to liver cells in vitro and in vivo. *Bioconjugate Chemistry*, 24(3), 314–332.[CrossRef].
- Kozubek, P. A., & B. M. (2013). BioImage Informatics Index (BIII).
- Lakowicz, J. R. (1999). *Principles of fluorescence microscopy*. (3rd ed). Springer.
- Li, L., Görgens, A., Mussack, V., Pepeljdjyska, E., Hartz, A. S., Rank, A., Schmohl, J., Krämer, D., El Andaloussi, S., Pfaffl, M. W., & Schmetzer, H. (2022). Description and optimization of a multiplex bead-based flow cytometry method (MBFCM) to characterize extracellular vesicles in serum samples from patients with hematological malignancies. *Cancer Gene Therapy*, 29, 1600–1615.[CrossRef].
- Martín-Cófreces, N. B., Torralba, D., Lozano-Prieto, M., Fernández-Gallego, N., & Sánchez-Madrid, F. (2021). TIRF microscopy as a tool to determine exosome composition. *Methods in Molecular Biology*, 2346, 91–104.[CrossRef].
- Mastrorarde, D. N. (2005). Automated electron microscope tomography using robust prediction of specimen movements. *Journal of Structural Biology*, 152(1), 36–51.[CrossRef].

- Melling, G. E., Conlon, R., Pantazi, P., Dellar, E. R., Samuel, P., Baena-Lopez, L. A., Simpson, J. C., & Carter, D. R. F. (2022). Confocal microscopy analysis reveals that only a small proportion of extracellular vesicles are successfully labelled with commonly utilised staining methods. *Scientific Reports*, *12*(1), 262.[CrossRef].
- Mével, M., Kamaly, N., Carmona, S., Oliver, M. H., Jorgensen, M. R., Crowther, C., Salazar, F. H., Marion, P. L., Fujino, M., & Natori, Y. (2010). DODAG; A versatile new cationic lipid that mediates efficient delivery of pDNA and siRNA. *Journal of Controlled Release*, *143*(2), 222–232.[CrossRef].
- Michel, T., Luft, D., Abraham, M. - K., Reinhardt, S., Salinas Medina, M. L., Kurz, J., Schaller, M., Avci-Adali, M., Schlensak, C., Peter, K., Wendel, H. P., Wang, X., & Krajewski, S. (2017). Cationic nanoliposomes meet mRNA: Efficient delivery of modified mRNA using hemocompatible and stable vectors for therapeutic applications. *Molecular Therapy - Nucleic Acids*, *8*, 459–468.[CrossRef].
- Mills-Goodlet, R., Johnson, L., Hoppe, I. J., Regl, C., Geppert, M., Schenck, M., Huber, S., Hauser, M., Ferreira, E., Hüsing, N., Huber, C. G., Brandstetter, H., Duschl, A., & Himly, M. (2021). The nanotopography of SiO₂ particles impacts the selectivity and 3D fold of bound allergens. *Nanoscale*, *13*(48), 20508–20520.[CrossRef].
- Mizenko, R. R., Brostoff, T., Rojalin, T., Koster, H. J., Swindell, H. S., Leiserowitz, G. S., Wang, A., & Carney, R. P. (2021). Tetraspanins are unevenly distributed across single extracellular vesicles and bias sensitivity to multiplexed cancer biomarkers. *Journal of Nanobiotechnology*, *19*(1), 250.[CrossRef].
- Nanoimager. Nanoimager. Available from: <https://oni.bio/nanoimager/>
- Nanoview. Nanoview. Available from: <https://www.nanoviewbio.com/>
- Nikoloff, J. M., Saucedo-Espinosa, M. A., Kling, A., & Dittrich, P. S. (2021). Identifying extracellular vesicle populations from single cells. *Proceedings of the National Academy of Sciences of the United States of America*, *118*(38), e2106630118.[CrossRef].
- Nolte, H., Macvicar, T. D., Tellkamp, F., & Krüger, M. (2018). Instant clue: A software suite for interactive data visualization and analysis. *Scientific Reports*, *8*(1), 12648.[CrossRef].
- Qin, X., Lin, X., Liu, L., Li, Y., Li, X., Deng, Z., Chen, H., Chen, H., Niu, Z., Li, Z., & Hu, Y. (2021). Macrophage-derived exosomes mediate silica-induced pulmonary fibrosis by activating fibroblast in an endoplasmic reticulum stress-dependent manner. *Journal of Cellular and Molecular Medicine*, *25*(9), 4466–4477.[CrossRef].
- Riazanski, V., Mauleon, G., Lucas, K., Walker, S., Zimnicka, A. M., Mcgrath, J. L., & Nelson, D. J. (2022). Real time imaging of single extracellular vesicle pH regulation in a microfluidic cross-flow filtration platform. *Communications Biology*, *5*(1), 13.[CrossRef].
- Ricklefs, F. L., Maire, C. L., Reimer, R., Dührsen, L., Kolbe, K., Holz, M., Schneider, E., Rissiek, A., Babayan, A., Hille, C., Pantel, K., Krasemann, S., Glatzel, M., Heiland, D. H., Flitsch, J., Martens, T., Schmidt, N. O., Peine, S., Breakefield, X. O., & Lamszus, K. (2019). Imaging flow cytometry facilitates multiparametric characterization of extracellular vesicles in malignant brain tumours. *Journal of Extracellular Vesicles*, *8*(1), 1588555.[CrossRef].
- Saha, R., Verbanic, S., & Chen, I. A. (2018). Lipid vesicles chaperone an encapsulated RNA aptamer. *Nature Communications*, *9*(1), 2313.[CrossRef].
- Silva, A. M., Lázaro-Ibáñez, E., Gunnarsson, A., Dhande, A., Daaboul, G., Peacock, B., Osteikoetxea, X., Salmond, N., Friis, K. P., Shatnyeva, O., & Dekker, N. (2021). Quantification of protein cargo loading into engineered extracellular vesicles at single-vesicle and single-molecule resolution. *Journal of Extracellular Vesicles*, *10*(10), e12130.[CrossRef].
- Smal, I., Loog, M., Niessen, W., & Meijering, E. (2010). Quantitative comparison of spot detection methods in fluorescence microscopy. *Ieee Transactions on Medical Imaging*, *29*(2), 282–301.[CrossRef].
- Strohmeier, K., Hofmann, M., Hauser, F., Sivun, D., Puthukodan, S., Karner, A., Sandner, G., Le Renard, P. -E., Jacak, J., & Mairhofer, M. (2021). CRISPR/Cas9 genome editing vs. over-expression for fluorescent extracellular vesicle-labeling: A quantitative analysis. *International Journal of Molecular Sciences*, *23*(1), 282.[CrossRef].
- Su, Y., Kumar, A., & Deep, G. (2022). Characterization of exosomal surface proteins by immunogold labeling. *Methods in Molecular Biology*, *2413*, 177–182.
- Sung, B. H., Ketova, T., Hoshino, D., Zijlstra, A., & Weaver, A. M. (2015). Directional cell movement through tissues is controlled by exosome secretion. *Nature Communication*, *6*, 7164.[CrossRef].
- Sung, B. H., Von Lersner, A., Guerrero, J., Krystofiak, E. S., Inman, D., Pelletier, R., Zijlstra, A., Ponik, S. M., & Weaver, A. M. (2020). A live cell reporter of exosome secretion and uptake reveals pathfinding behavior of migrating cells. *Nature Communication*, *11*(1), 2092.[CrossRef].
- Tertel, T., Görgens, A., & Giebel, B. (2020). Analysis of individual extracellular vesicles by imaging flow cytometry. *Methods in Enzymology*, *645*, 55–78.[CrossRef].
- Tertel, T., Schoppet, M., Stambouli, O., Al-Jipouri, A., James, P. F., & Giebel, B. (2022). Imaging flow cytometry challenges the usefulness of classically used extracellular vesicle labeling dyes and qualifies the novel dye Exoria for the labeling of mesenchymal stromal cell-extracellular vesicle preparations. *Cytotherapy*, *24*(6), 619–628.[CrossRef].
- Tian, T., Wang, Y., Wang, H., Zhu, Z., & Xiao, Z. (2010). Visualizing of the cellular uptake and intracellular trafficking of exosomes by live-cell microscopy. *Journal of Cellular Biochemistry*, *111*(2), 488–496.[CrossRef].
- Tsuji, G., Fujii, S., Sunami, T., & Yomo, T. (2016). Sustainable proliferation of liposomes compatible with inner RNA replication. *Proceedings of the National Academy of Sciences of the United States of America*, *113*(3), 590–595.[CrossRef].
- Tyanova, S., Temu, T., Sinitcyn, P., Carlson, A., Hein, M. Y., Geiger, T., Mann, M., & Cox, J. (2016). The Perseus computational platform for comprehensive analysis of (prote)omics data. *Nature Methods*, *13*(9), 731–740.[CrossRef].
- Verweij, F. J., Balaj, L., Boulanger, C. M., Carter, D. R. F., Compeer, E. B., D'Angelo, G., El Andaloussi, S., Goetz, J. G., Gross, J. C., Hyenne, V., Krämer-Albers, E. -M., Lai, C. P., Loyer, X., Marki, A., Momma, S., Nolte-’t Hoen, E. N. M., Pegtel, D. M., Peinado, H., Raposo, G., & Van Niel, G. (2021). The power of imaging to understand extracellular vesicle biology in vivo. *Nature Methods*, *18*(9), 1013–1026.[CrossRef].
- Verweij, F. J., Bebelman, M. P., Jimenez, C. R., Garcia-Vallejo, J. J., Janssen, H., Neeffjes, J., Knol, J. C., De Goeij-De Haas, R., Piersma, S. R., Baglio, S. R., Verhage, M., Middeldorp, J. M., Zomer, A., Van Rheenen, J., Coppolino, M. G., Hurbain, I., Raposo, G., Smit, M. J., Toonen, R. F. G., ... Pegtel, D. M. (2018). Quantifying exosome secretion from single cells reveals a modulatory role for GPCR signaling. *Journal of Cell Biology*, *217*(3), 1129–1142.[CrossRef].
- Welsh, J. A., Van Der Pol, E., Arkesteijn, G. J. A., Bremer, M., Brisson, A., Coumans, F., Dignat-George, F., Duggan, E., Ghiran, I., Giebel, B., Görgens, A., Hendrix, A., Lacroix, R., Lannigan, J., Libregts, S., Lozano-Andrés, E. - A., Morales-Kastresana, A., Robert, S., De Rond, L., & Jones, J. C. (2020). MIFlowCyt-EV: A framework for standardized reporting of extracellular vesicle flow cytometry experiments. *Journal of Extracellular Vesicles*, *9*(1), 1713526.[CrossRef].
- Wiklander, O. P. B., Brennan, M., Lötval, J., Breakefield, X. O., & El Andaloussi, S. (2019). Advances in therapeutic applications of extracellular vesicles. *Science Translational Medicine*, *11*(492), eaav8521.[CrossRef].
- Willms, E., Cabañas, C., Mäger, I., Wood, M. J. A., & Vader, P. (2018). Extracellular vesicle heterogeneity: Subpopulations, isolation techniques, and diverse functions in cancer progression. *Frontiers in Immunology*, *9*, 738.[CrossRef].
- Wolf, M., Poupardin, R. W., Ebner-Peking, P., Andrade, A. C., Blöchl, C., Obermayer, A., Gomes, F. G., Vari, B., Maeding, N., Eminger, E., Binder, H. - M., Raninger, A. M., Hochmann, S., Bracht, G., Spittler, A., Heuser, T., Ofir, R., Huber, C. G., Aberman, Z., & Strunk, D. (2022). A functional corona around extracellular vesicles enhances angiogenesis, skin regeneration and immunomodulation. *Journal of Extracellular Vesicles*, *11*(4), e12207.
- Wu, S. Y., Putral, L. N., Liang, M., Chang, H. - I., Davies, N. M., & Mcmillan, N. A. J. (2008). Development of a novel method for formulating stable siRNA-loaded lipid particles for in vivo use. *Pharmaceutical Research*, *26*(3), 512.[CrossRef].

SUPPORTING INFORMATION

Additional supporting information can be found online in the Supporting Information section at the end of this article.

How to cite this article: Schürz, M., Danmayr, J., Jaritsch, M., Klinglmayr, E., Benirschke, H. M., Matea, C. - T., Zimmerebner, P., Rauter, J., Wolf, M., Gomes, F. G., Kratochvil, Z., Heger, Z., Miller, A., Heuser, T., Stanojlovic, V., Kiefer, J., Plank, T., Johnson, L., Himly, M., ... Meisner-Kober, N. (2022). EVAnalyzer: High content imaging for rigorous characterisation of single extracellular vesicles using standard laboratory equipment and a new open-source ImageJ/Fiji plugin. *Journal of Extracellular Vesicles*, 11, e12282. <https://doi.org/10.1002/jev2.12282>